WALL HEAT TRANSFER PROPERTIES OF METAL MICROFIBER CATALYST SUPPORT STRUCTURES

by

Carlos Francisco Gonzalez

A thesis submitted to the Graduate Faculty of
Auburn University
in partial fulfillment of the
requirements for the Degree of
Master of Science

Auburn, Alabama
May 9th, 2015

Approved by

Bruce. J Tatarchuk, Chair, Charles E. Gavin III Professor
Steve R. Duke, Alumni Associate Professor
William R. Ashurt, Associate Professor

Abstract

A renewed interest in highly exothermic and endothermic reactions for scalable energy technology have demanded a need for a catalyst support structure that is capable of managing the thermal requirements of the reaction while promoting a high level of reaction efficiency. A novel catalyst support structure Microfibrous Entrapped Catalysts (MFEC) consists of a sintered network of highly thermally conductive micron-diameter metal fibers that entrap catalyst particles. The MFEC's thermal properties and tube-wall interactions were studied to quantify and predict effective thermal conductivities and wall heat transfer coefficients.

Various fiber diameters were tested at the same volume percent (8.8 vol%) and gave thermal conductivities in a range of 3.15 to 6.80 $[Wm^{-1}K^{-1}]$ and wall contact conductances in a range of 712 to 2939 $[Wm^{-2}K^{-1}]$. Stainless steel tubes were lathed with an internal screw pattern to give additional surface area (up to 41.6%) for the MFEC to contact the tube wall. In all tests, the MFEC was determined to have fibers that were unable to elastically conform to the grooves cut into the tube wall, leading to a reduction of the wall heat transfer coefficient by approximately 61%. Flowing gas tests were also utilized showing wall heat transfer coefficients up to 350 $[Wm^{-2}K^{-1}]$ at a GHSV of 13,700 $[h^{-1}]$. Metal volume percent was kept constant for all fiber diameters. Using a thermal interface material tester was used to test the axial properties of the MFEC. Axial thermal conductivities ranged from 0.320 to 0.493 $[Wm^{-1}K^{-1}]$, and confirmed using a thermal effusivity tester. Thermal resistance network diagrams were constructed to show that wall heat transfer coefficient is limited by the thermal conductivity of the interstitial gap.

Once the interstitial fluid's thermal resistance is greater than 2.07E-4 [K/W], the stainless steel wall becomes the limiting step.

Acknowledgments

First, I would like to thank the Micro-Nano REU program at Auburn for giving me an opportunity in 2008 to experience research on a graduate level and inspiring me to continue in my education. Specifically I would like to thank Dr. Mark Byrne, Dr. Steve Duke and Dr. Bart Prorok.

Second, I would like to thank my advisor, Dr. Bruce Tatarchuk for all he taught me and for the various members of CM3 that supported my work as well. I would like to thank Rob Yantz for all of his help with my research and all of the insightful discussions we had that lead to many creative ideas and methodologies used in this thesis. I would like to thank Dr. Roy Knight, Dr. Wen-hua Zhu, Melissa Peacock, Brian Schwieker, MariAnne Sullivan for all of their contributions towards my work.

Finally, and most importantly, I would like to thank my family and friends. Without them, I would have never been able to accomplish all that I did at Auburn. When I didn't believe in myself, they did and kept pushing me forward. I am very grateful to them for not letting me give up. I would also like to thank my band, Point of Sizzle and all of the supportive fans we had. The experience I had through music will continue to inspire me for the rest of my life.

Table of Contents

List of Tables

List of Figures

List of Abbreviations and Symbols

Abbreviations

- AWG – American Wire Gauge
- CFD – Computational Fluid Dynamics
- DME – Dimethyl Ether
- FTS – Fischer Tropsch Synthesis
- ID – Inner Diameter
- INF – Infinite
- MFEC – Microfibrous Entrapped Catalysts
- SEM – Scanning Electron Microscope
- TIM – Thermal Interface Material
- UHP – Ultra High Purity

Symbols

- c_p – Heat Capacity (constant pressure)
- $\dot{m}$ – Mass Flow Rate
- Fo – Fourier Number
- h - Contact Conductance, Heat Transfer Coefficient
- A – Area
- P – Pressure
- Q – Heat Flux
- R – Thermal Resistance
- T – Temperature
- e – Thermal Effusivity
- k – Thermal Conductivity
- r – Radial Position
- x – Sample Thickness
- α – Thermal Diffusivity
- ρ – Density
- φ – Volume Fraction
- χ – Mass Fraction
- ϵ – Surface Roughness

Subscripts

- ∞ - Heat Sink Location
- cold – Cold
- conv – Convection
- eff – Effective
- fibers – Fibers
- fluid – Fluid
- g – Gas
- gas – Gas
- hot – Hot
- i – Node "I", inside
- inlet – Inlet
- m – Mean
- MFEC – MFEC
- n – Node "n"
- o - Outside
- outlet – Outlet
- p – Pressure
- s – Solid
- SS – Stainless Steel
- w - Wall

CHAPTER 1

1. INTRODUCTION

This thesis presents the development of an approach to quantify the thermal properties of anisotropic, metallic fibrous materials and the interaction of the fiber to tube wall contact. The specific properties of interest are the effective thermal conductivity (k_{eff}) of the fiber matrix, the effective thermal contact resistance (R_{eff}) of the fiber matrix to the tube wall and the effect of tube roughness (ϵ) on the thermal contact resistance at the wall. The hypothesis is by utilizing both transient conduction and steady-state conduction experiments, that the wall heat transfer can be fundamentally separated into the fluid-phase heat transfer and the wall-fiber heat transfer. Methods used will include a transient radial conduction analysis, a steady-state thermal interface testing apparatus that follows ASTM D-5470 to determine axial conduction. These techniques allow for a systematic approach to determining and isolating the individual heat pathways in the metallic fibrous materials.

1.1 Research Motivation

A renewed interest in highly exothermic and endothermic reactions such as Fischer Tropsch Synthesis (FTS), dimethyl ether (DME) and ammonia synthesis for scalable energy technology have demanded a need for a catalyst support structure that is capable of handling the thermal requirements of the reaction while promoting a high level of reaction efficiency. Typical methods for managing the transfer of heat include small diameter multi-tubular fixed reactors [1] and [2], slurry reactors [3] and [4], and high gas-recycle using commercially available catalyst pellets. While the fixed bed allows for the reaction to run successfully, it does not promote high efficiency per-pass in the reactor due to poor mass transfer characteristics of large catalyst particles. As for the slurry-phase or fluidized bed solution, there is a significant amount of

separation and downstream processing required due to the residence time distribution in the reactor. A novel catalyst structure using micron-diameter metal fibers (referred to as Micro-Fibrous Entrapped Catalyst, or MFEC) has been developed to "entrap" small catalyst particles within the sintered fiber matrix [5]. This multi-functional support structure allows for commercial catalysts to be used while promoting high thermal management and high mass transfer. Successful tests of the MFEC support structure using FTS were demonstrated by Sheng et al. (2012) in large diameter tubes (15mm and 41mm inner diameter) [6]. The success of the experiment was largely due to the metal fiber's ability to transport the heat generated on the surface of the catalyst particle into the MFEC structure and out of the reactor. Typical fixed bed or packed bed reactors use catalysts that have limited contact between themselves as well as the reactor wall. This can cause large amounts of heat to accumulate within the reactor due to the lack of an efficient way to transport the heat out of the reactor.

1.2 Traditional Reactor Thermal Management Solutions

Since highly exothermic and endothermic reactions require reactors with high rates of heat transfer through the reactor wall, many traditional reactor styles have been adjusted to meet the design requirements. For fixed bed or packed bed reactors, a tube is loaded with commercially available catalyst pellets and the reactants are passed through the bed. Catalyst pellets are typically on the magnitude of a few millimeters to optimally avoid fluid channeling and to keep the reactor pressure drop as low as possible. The disadvantage to larger catalyst pellets is the decrease in mass transfer for the reactants to reach the catalyst surface compared to smaller catalyst particles. Using small diameter tubes require a large array of tubes in an outer shell that act like a shell and tube heat exchanger. This configuration provides very poor efficiency per-pass due to the small volumetric catalyst loading, requiring that the unused

reactants be recycled. Because the tubes were so small (< 7mm), the temperature was controlled

sufficiently to yield enough product with an acceptable product selectivity (in FTS, the product

selectivity is strongly dependent upon reaction temperature) [7]. If too much heat is generated

within the reaction, methanation (syngas converted to methane) or thermal runaway can occur.

Another method of managing exothermic reactions would be to create a slurry-phase

reactor. This type of design offers the ability to use the convective heat transfer properties of the

slurry to create an effective wall heat transfer coefficient of up to 5000 $W/m^2 \cdot K$ [8]. This

solution also offers a high mass transfer rate at the catalyst particle surface due to the constant

churning of the reactants in the slurry bed, liquid as the surrounding fluid and the small size of

the catalyst particles. Although slurry-phase beds present tremendous advantages to solving the

heat transfer problems with highly exothermic gas-to-liquid reactions, Davis (2005) mentions

that fixed bed reactors remain an attractive approach because they have the highest volumetric

catalyst loading and the highest potential volumetric productivity [9]. The major challenge to

making the fixed-bed reactor a practical option are the small wall heat transfer coefficients and

poor intra-bed thermal conductivities. It was calculated that for a tube diameter of 127mm ID

that 68.8% of the overall thermal resistance was from the inner wall contact resistance [6].

1.3 Fundamentals of Contact Conductance

Since most materials do not have perfectly smooth surfaces, there is a thermal resistance

between the two solids in contact. Usually a gas or fluid will occupy the space in between the

two solids, which can comprise a significant portion of the thermal resistance of the gap,

depending on the roughness of the two surfaces in contact. A visual representation of the solid

contacts and interstitial fluid can be seen in Figure 1-1. Other than the surface roughness and the

interstitial fluid's thermal properties, the pressure applied to the two solids is extremely

important as well as the hardness of the two materials in contact. The pressure applied and the material hardness are complimentary because of the surfaces' ability to deform and conform to each other. For example, if a soft malleable material is pressed against a hard rigid material, the softer material will deform and conform to the surface topography of the hard surface, thus creating more solid-to-solid contact between the surfaces.
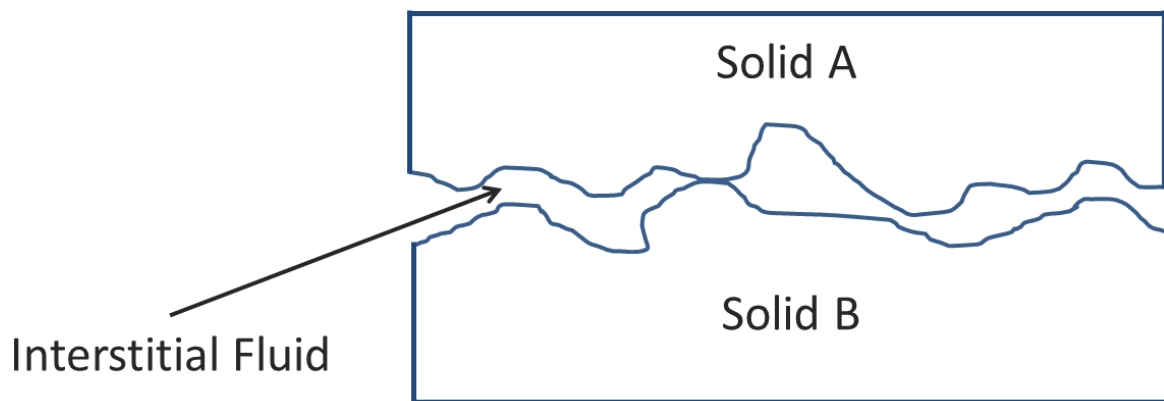
Figure 1-1: Representation of two rough solid surfaces in contact with each other. The interstitial fluid resides within the space between the two sold surfaces.

Other than the conduction pathway through the solid contact points, the transfer of heat through the interstitial gap is a significant portion of the total heat transferred through the joint [10]. Since the scale length of the gap between the two surfaces is generally on the order of 1μm, convection currents are unable to be established. Radiation plays a significant role at temperatures exceeding 300°C, unless the temperature difference across the gap allows for radiation to take a significant role [10]. Therefore, it is assumed that conduction across the gap is the primary mode of heat transfer in most cases. Contact conductance (h) is defined as the

ratio of heat flux (Q/A) to the temperature across the gap as seen in Eq. (1.1), and thermal

resistance (R) is defined as the inverse of contact conductance as seen in Eq. (1.2).

$$h = Q/(A\Delta T) \tag{1.1}$$

$$R = A\Delta T/Q \tag{1.2}$$

Since these two equations deal with the bulk transfer of heat between the two solids, there

needs to be separate equations that govern the heat transfer through the interstitial material and at

the points where the two solid surfaces are in direct contact. The total heat flow (Q) can be

separated into the conduction through the direct solid contacts (Q_s) and the interstitial fluid (Q_g)

as seen in Eq. (1.3).

$$Q = Q_s + Q_g \tag{1.3}$$

where,

$$Q_s = A\Delta T/h_s \tag{1.4}$$

$$Q_g = A\Delta T/h_g \tag{1.5}$$

The solid contact conductance (h_s) and the gap conductance (h_g) are additive to form the total

contact conductance as seen in Eq. (1.1). These equations form the mathematical basis for

investigating the improvement in contact conductance by altering the interstitial gap material or

improving the solid contacts between the two surfaces.

Within the past 60 years, several methods to decrease the thermal resistance (or increase

the thermal conductance) across the gap have been investigated. Most of these methods involve

replacing of the fluid gap with a solid interstitial material. Since a solid material has a higher

thermal conductivity than the fluid gap, it is a suitable choice for replacement. However, the material must also deform well against the surfaces of the two solids in contact. Several interstitial materials would include foils, wire screens and thermally conductive fluids or greases [10].

Foils are typically made of very soft, malleable metals that help to deform to the solid surfaces in contact, creating additional solid contacts. Several independent studies reported experimental values for the contact conductance with and without the foil in a vacuum as seen in Table 1-1 [11] and [12]. Depending on the foil's thermal conductivity, thickness and the pressure applied at the joint, the increase in the contact conductance was up to 6 times greater than without the foil. The main conclusions drawn from these studies indicate that:

1) The foil provides a significant increase in contact conductance in the presence of a vacuum.

2) As the hardness of the foil decreased, the increase in contact conductance using the foil was increased.

3) The foil was more effective at increasing the contact conductance between rougher surfaces than smoother surfaces (depending on the optimum thickness of the foil). This is due to the increase in the effective surface area in between the two surfaces in contact.

Reference	Foil and foil thickness (µm)	Contact Pressure (kPa)	Surface roughness (µm) rms	Flatness Deviation (µm)	Contact conductance (W/m²·K) bare junction	Contact conductance (W/m²·K) With foil
[11]	Lead (200)	69	1.50-2.00	1125	190	730
[11]	Lead (200)	207	1.50-2.00	1125	300	830
[11]	Aluminum (50)	69	12-16	425	265	390
[11]	Aluminum (50)	207	12-16	425	465	665
[12]	Indium (25)	276	0.30-0.45	0.875	2270	13060
[12]	Indium (25)	276	1.15-1.25	0.625	2780	21580
[12]	Indium (25)	552	0.30-0.45	0.875	3520	18740
[12]	Indium (25)	552	1.15-1.25	0.625	4540	27260

Table 1-1 Effect of surface texture on contact conductance with a filler material [10]

The other important factors that influence the increases in contact conductance would be the foil thickness and the hardness of the metal foil. There is an optimal thickness for each foil to be used because if the foil is too thin it doesn't provide enough material to fill the interstitial gap, where as if a foil is too thick it will be unable to deform well to the surfaces. More important than the material's thermal conductivity or the thickness of the foil, is the hardness of the material. In a study of copper, aluminum, lead and indium foils it was found that lead and indium had better contact conductance than both aluminum and copper [13]. It was concluded that the most important factor in the enhancement of contact conductance was the hardness of the material used.

Wire screens were investigated in 1962 by Fried and Costello as a method for improving the contact conductance between two solid surfaces [11]. Their experiments concluded that the wire screens added additional thermal resistance due to the reduced contact area between the two surfaces. An additional study by Gyorog in 1971 using stainless steel and titanium wire meshes, confirmed that there was an increase in thermal resistance by using screens [14]. The study further concluded that coarse meshes add higher resistances than finer meshes, which is related to the amount of surface area that the screen is in contact with. Another experimental study by

Cividino and Yovanovich in 1975 investigated copper screens with stainless steel surfaces [15]. This study found that the thermal resistance decreased in the presence of a vacuum but decreased in air. An additional conclusion was made that showed copper screens (or gauze) were a good choice for surfaces that were poorly mated to each other, but that it did not always decrease the overall resistance.

Thermal greases were studied as a method for improving thermal contact conductance by replacing the interstitial fluid with a grease or paste. The thermal conductivity of greases is typically orders of magnitude greater than that of air. Studies by Sauer et al. (1971) and Chung et al. (1992) showed that the additional conduction pathway is capable of increasing the thermal contact conductance by 8-70% for two surfaces in a vacuum and 0-60% in air [16], [17]. While thermal greases are excellent replacements for the interstitial fluid, the volatile components of the mixture may evaporate over time, thus leading to decreased performance over time.

1.4 Development of Microfibrous Entrapped Catalysts

The fibers that compose the metallic metal structure of MFEC are manufactured in a bundle drawn process. This process allows metallic wire to be drawn down to less than 25 microns in diameter without the need for specialized dies and drawing methods. Common example materials that can be drawn are certain polymers, glass, stainless steel, nickel and copper. Upon completion on the fiber manufacturing process the metal fibers are dispersed in water along with cellulose and are sent through a conventional wet-lay paper-making machine. This wet-lay process allows for the MFEC to be easily scaled and mass produced using currently available technology. The added cellulose acts as a binder for holding the metal fibers together when dried. Once the sheet has been dried, it is sent to an oxidizing furnace to remove the cellulose by low-oxygen combustion (5% O_2 in N_2). The remaining structure has significant

void space between the fibers which will allow for the entrapment of catalyst particles. Before the entrapment step, the metal fibers must be joined together. In a large belt furnace, the fibers are sintered together in a reducing environment at approximately 750 to 800°C. The end result is a sintered fiber network that is ready to accept catalyst particles.

The entrapment of the catalyst particles involves the dispersion of fine mesh particulates into the metal fiber matrix. These particulates can easily be produced by traditional incipient wetness impregnation or by simply crushing pre-manufactured catalyst pellets and sieving them down to the required size. There are a few factors that determine the required particle size to entrap within the "effective cages" created in the metal fiber matrix [18]. Once the particles are dispersed into the matrix, the sheet is pressed down from the top to plastically deform the structure to entrap the catalyst particles.   The fibers hold the catalyst particles in place while also providing direct contact for enhanced conduction heat transfer. An additional benefit to the suspension of catalyst particles in the fiber matrix is the increased mass transfer to and from the catalyst surface and the reduction of fluid channeling [19]. Once the catalyst has been successfully entrapped, the MFEC can be cut to any shape to fit inside a reactor. Since the metal fibers have been softened in the annealing process, the fibers can plastically deform up to the reactor wall to provide enhanced heat transfer compared to rigid ceramic-based catalyst particles.

1.5 Prior Research

A study designed to test the MFEC's ability to thermally stabilize a very exothermic reaction was tested by running FTS in 15mm and 41mm inner diameter reactors [6]. The intent was to show that even with an extremely high adiabatic temperature rise of 1600°C, the reaction could be thermally controlled in situations that would cause thermal runaway in traditional packed beds [20]. The study showed the radial temperature profiles of the reactor in both reactor

9

diameters running FTS using a packed bed and the MFEC. The MFEC was found to be 56 times more thermally conductive than a packed bed with equivalent particle size. Furthermore, FTS was successfully run with MFEC in both bed diameters, whereas the packed bed experienced thermal runaway leading to near-complete conversion of the syngas into methane and water.

An introductory study of the MFEC was also made to determine the thermal conductivity and wall heat transfer coefficient [21]. In this study, 12 micron fibers (copper, nickel and stainless steel fibers were all tested) were sintered together to form the metal support for alumina particles (180-250μm diameter). The MFEC was stamped out using a circular leather punch (oversized by 5% of inner tube diameter) and stacked into a copper tube. Fine wire thermocouples at known positions were used to measure the temperature rise as the tube was placed into a hot water bath. From these temperature profiles vs. time, the effective thermal conductivity and wall heat transfer coefficient were estimated using the Euler implicit method and a Newton-Raphson search algorithm. Experiments of flowing gas were also conducted to obtain steady-state temperature profiles. The objective of this test was to examine the wall heat transfer coefficient's dependence upon the Reynolds Number. These temperature profiles were fitted using the Euler explicit method and a Newton-Raphson search algorithm.

Other tests to improve the thermal conductivity of the MFEC were investigated further in a study by Sheng (2013) by testing the effect of sintering temperature and time on the effective thermal conductivity of the MFEC. It was hypothesized that the most important factor in the transport of heat through the MFEC was through the fiber-to-fiber "junctions" created during the sintering process. The MFEC was sintered at various temperature and times to test the effect of the sintering process on the effective thermal conductivity. The MFEC was electroplated in a copper ion solution and subsequently annealed at 750°C in an attempt to improve the sintered

fiber junctions. An incipient wetness impregnation of a copper ion solution of the MFEC followed by a subsequent annealing at 750°C was also tested to add additional copper to the junctions and improve the effective thermal conductivity. The study concluded that the following variables tested provided the best means to improve the thermal conductivity: sintering temperature > sintering time > electroplating > impregnation.

To further investigate the fundamental heat transfer properties of the MFEC, computational fluid dynamic (CFD) simulations were performed in a study by Sheng et al. (2013) to compare and quantify effective thermal properties for a simplified, ideal model of MFEC and a packed bed [19]. The advantage of this study was to obtain micro-scale temperature measurement, which allowed a unique approach to the micro-scale heat transfer properties of the MFEC and packed bed. Under stagnant and flowing gas conditions temperature and velocity (flowing gas only) profiles were obtained and analyzed for quantitative and qualitative data. The study concluded that the 90% of the thermal resistance to heat flow in a packed bed is due to the poor solid-to-solid contact between particles. For the MFEC, it was found that 97.2% of all the heat flow occurred within the continuous fiber cylinders that were used to mimic the micro metal fibers in the MFEC bed.

1.6 Research Objectives

In a recent study of FTS using MFEC by Sheng et al. (2012), the limiting step in thermal management was the contacting of the MFEC with the reactor wall [6]. The knowledge of how the MFEC contacts surfaces is needed to allow future improvements. The simplest variable to change in the MFEC is the diameter of the fibers that compose the fiber matrix. A thermal interface tester (ASTM D-5470) was used to determine the contacting efficiency of various fiber diameters (as well as fiber blends) to provide the thermal conductivity of the sintered fiber

matrix. Contact pressures and sample thicknesses were varied to determine the contributions of both the thermal conductivity of the material as well as its ability to contact the surface of a reactor wall.

To obtain the radial effective thermal conductivity and wall heat transfer coefficient, the MFEC will be tested using the transient tube tests that Sheng (2013) used [22].   A MATLAB simulation will be used to mathematically obtain best-fit parameters for the effective thermal conductivity and the wall heat transfer coefficient (contact conductance). The variables to be tested by this method in this study will be the effect of fiber diameter, the effect of the interstitial fluid within the MFEC and the effect of tube roughness on the thermal properties (k_{eff}, h).

Using these testing methods, the effective thermal parameters for the MFEC can be determined and an analysis can be performed to extract individual properties from the bulk material properties of the MFEC. The individual contributions will form a qualitative understanding of how heat is transferred through the wall and into the MFEC as well as provide a quantitative analysis to aid in future reactor design. An ability to estimate effective thermal parameters for reactor design will ultimately be the goal of this thesis.

CHAPTER 2

2. EXPERIMENTAL EQUIPMENT AND METHODS

2.1 MFEC Sample Preparation

The copper fibers used to create the matrix structure of the MFEC were purchased from IntraMicron (Auburn, AL). The fibers ordered were near-cylindrical, having a diameter of 12 microns and a length of 5mm. The fibers arrived in buckets of a diluted acetic acid solution to prevent the fibers from oxidizing. Once the fibers were ready to be processed, the dilute acetic acid solution was first washed from the fibers using water. The fibers were initially entangled with each other in massive "clumps" that needed to be pulled apart before they were to be processed. The pulled fibers were left to sit out for 24 hours to dry and oxidize. It was hypothesized that the oxide layer that developed during this time allowed for the fibers to better disperse during the wet-lay process. During experimentation, it was found that the fibers appeared to disperse more uniformly when oxidized than when they were not oxidized. Once the fibers were oxidized, they turned a deep purple/brown color indicating they were ready for the wet-lay process.

First, the fibers were re-wetted before they were weighed. On average, the wetted 12 micron fibers were approximately 45% water and 55% fiber by weight. The fibers were then weighed out in a 13.5:1 ratio of fibers to cellulose. Cellulose acted as a binder and held the fibers together until they could be sintered together. The cellulose and fibers were put into a 1 gallon blender with water and blended on a "low speed" setting for 1 minute and 45 seconds. The mixture was then poured into a cylindrical "hand-sheet" mold. The mixture was agitated for approximately 15 seconds by hand and then the water was quickly drained. The hand sheet was

13

then transferred to a large sheet of cellulose to dry for 24 hours. The hand sheets were then set aside to be prepared for pre-sintering oxidation.

When the hand sheets were ready to be oxidized, the low-oxygen oven (Grieve NT-1000) was preheated to approximately 450°C. To ensure proper flow of gas through the oven, the exhaust fan was turned on and nitrogen gas and air were mixed and flowed into the oven. The mixture of air and nitrogen was mixed by a flow rate of 50mL/min of nitrogen and 40mL/min of air (approximately 9% O_2). The nitrogen used was cylinder air (UHP) and the air used was compressed air. The sheets were wrapped in woven carbon fiber cloth (FM10-250 by Calgon Carbon) and placed onto a stainless steel mesh screen. The carbon cloth prevented the sheets from sintering to the stainless steel screen or the sintering furnace belt. The sheets were then placed into the oven and remained in the oven for 30 minutes. At this point, all of the cellulose should have been burnt off and the sheets were removed. Since the cellulose was no longer binding the fibers together, the sheet was extremely brittle and was handled very delicately. Ideally, the sheets were immediately placed onto the sintering furnace belt to be sintered, but some were stored briefly before being sintered.

The sintering furnace (Model TCA144-9-108E81, Serial #AUA-1 by BTU International Inc.) was powered on prior to running samples. The furnace has a controllable temperature profile within it as well as a controllable belt speed. During the start-up period (8 hours), the furnace was heated up to the set temperature profile under flowing nitrogen. One hour prior to running the samples, the furnace was purged with a pre-set mixture of hydrogen and nitrogen. The furnace was profiled to give an average temperature of 775°C in the "heated zone" of the furnace and the belt speed was set to 7.62cm/min. This gave the samples approximately 36.7 minutes within the heated zone. More details about the sintering furnace are provided in Table

2-1. After sintering, the hand sheets were stored within plastic containers until needed for experimentation.

Zone #	1	2	3	4	5	6	7	8	9
Temperature [°C]	650	700	750	800	800	800	800	775	750

Table 2-1 Temperature settings of each zone within the sintering furnace during operation.

2.2 Radial Temperature Measurement Apparatus

In an effort to study and quantify the thermal conductivity and wall heat transfer coefficient of the MFEC, a simple experiment was designed. In order to measure the radial heat transfer coefficient and wall heat transfer coefficient, the MFM was inserted inside of a sealed tube and submersed in a hot water bath. Fine wire thermocouples were placed at precise locations along the radial profile recorded the temperature change with time. This temperature data formed the basis of the transient heat transfer analysis.

The tubes were purchased from Kurt Lesker (FN-0275) and are made of 316 stainless steel with CF vacuum flanges on both ends. The outer diameter of the tubes were 3.81 cm with an inner diameter of 3.50 cm, and were 12.54 cm from end to end. These tubes were designed to have the ability to pull a vacuum within the tube so that the interstitial fluid within the MFEC could be removed, isolating the heat transfer properties of the metal fibers. Both ends of the tube had a ¼" compression fitting welded to the caps of the tube (Kurt Lesker, Part # F0275N150NLN). This allowed for connections to various gas sources as well as the vacuum line. The assembled apparatus can be seen in Figure 2-4.
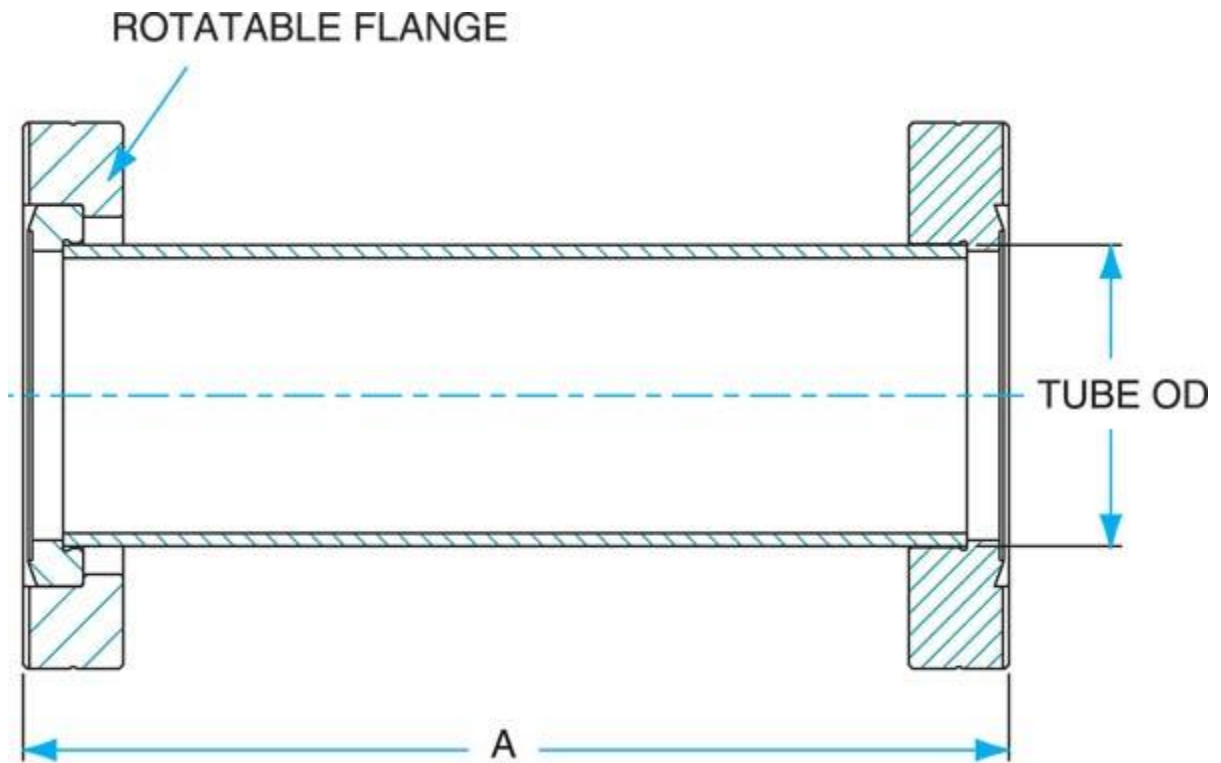
Figure 2-1- Schematic of Kurt Lesker Part# FN-0275 (A = 15.24 cm, Tube OD = 3.81 cm)

Figure 2-2 - Kurt Lesker Flange Cap (Part # F0275N150NLN)
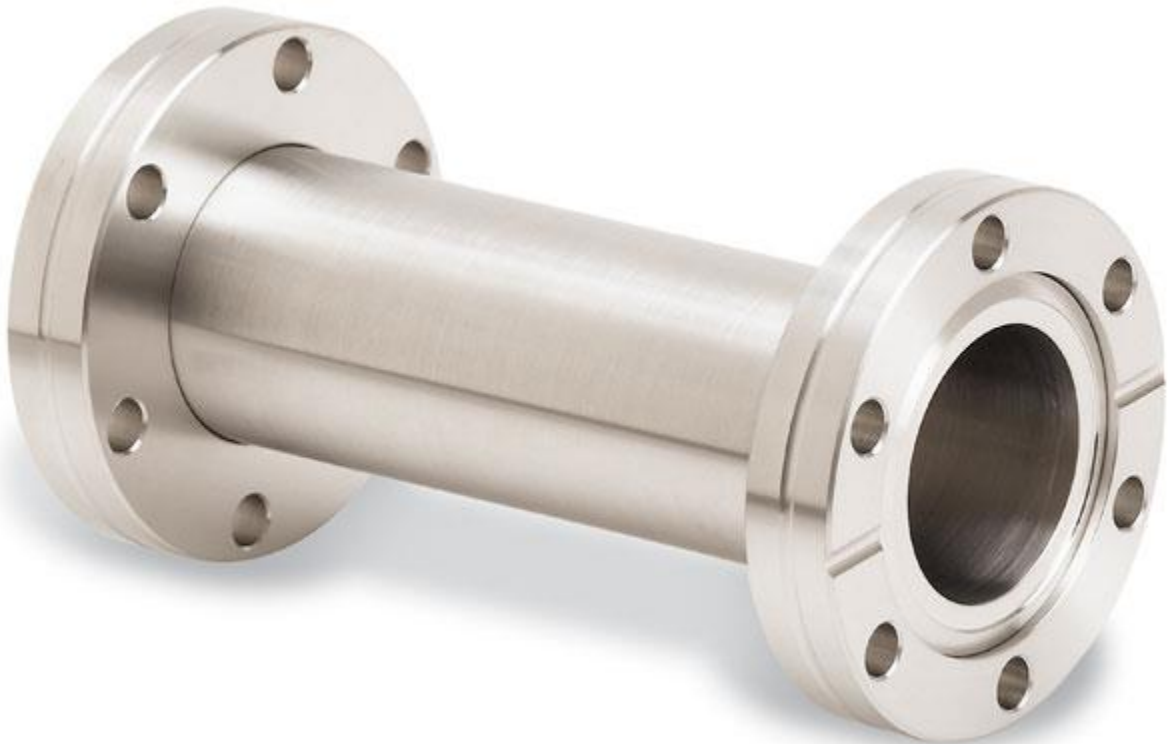
Figure 2-3 - Kurt Lesker CF Nipple (Part# FN-0275)
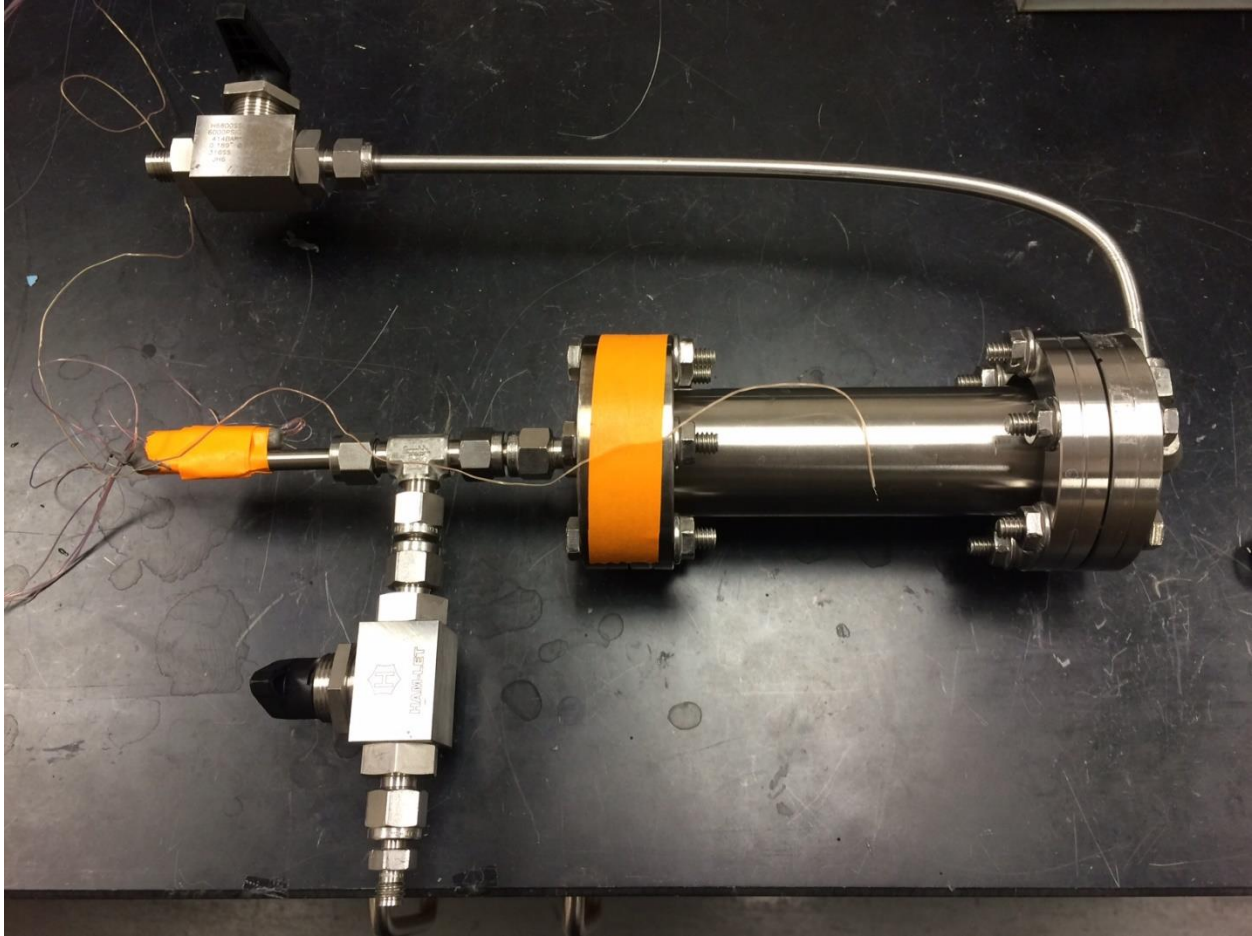
Figure 2-4 - Experimental apparatus used in radial heat transfer tests.

The thermocouples were purchased from Omega Engineering (Part # 5TC-TT-T-40-48). These thermocouples were 40 AWG (0.0799 mm), T-type (+/- 0.75% between -250 to 350°C) with a Teflon coating. Four thermocouples were used in the apparatus, one on the outside of the tube (to detect the moment the tube was submersed), and three thermocouples to measure the radial temperature profile. The thermocouples were fed into the apparatus through one the flange on the end of the tube. The radial positioning of the thermocouples can be seen in Figure 2-5. A data recorder (Omega Engineering OM-DAQPRO-5300 Serial # 312214) was used to record the temperature value of each thermocouple every second.

Thermocouple Locations

T1 – Centerline

T2 – Centerline + 0.635 cm

T3 – Centerline + 1.27 cm

T4 – On Outer Surface of Tube
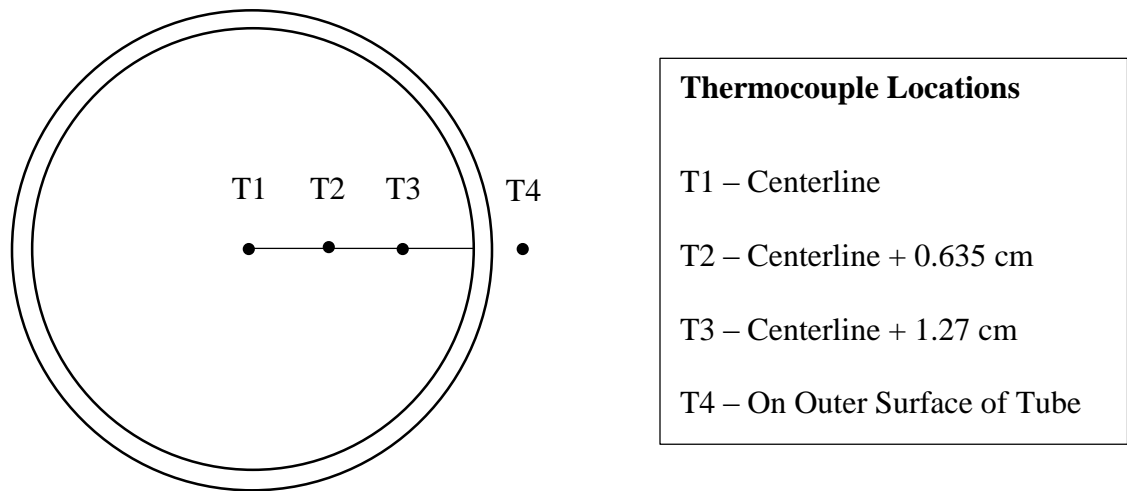
Figure 2-5 Thermocouple locations within radial temperature measurement apparatus.

The water bath used was a Thermo Precision General-Purpose Water Bath. While the unit was temperature controlled, the heating element was not designed for temperatures above approximately 75°C. The temperature was set to 99.9°C and the temperature was recorded using the external thermocouple on the experimental apparatus. To further enhance the heat transfer, a variable speed impellor was used to ensure that the water bath was a near-uniform temperature with a high convective external heat transfer coefficient.

The experiments carried out in this apparatus involved 6, 12 and 25 micron fibers that were punched out using a 3.4925 cm punch (2% oversized based on internal diameter) and stacked into the tube. The tube was packed to a length of 5cm (centered down the length of the tube) with quartz wool packed loosely on either end for thermal insulation (as seen in Figure 2-6). The thermocouple assembly was placed in the center of the tube and packing. The tube was sealed up with both flanges and prepared for experimentation. After the tube was sealed, a

rough vacuum (~50mTorr) was pulled on the tube to remove as much air as possible. If a gas

was to be used, the gas line was opened and purged through the tube for a period of 2 minutes.

The thermocouples were then plugged into the data logger and tested to confirm all

thermocouples were performing correctly.
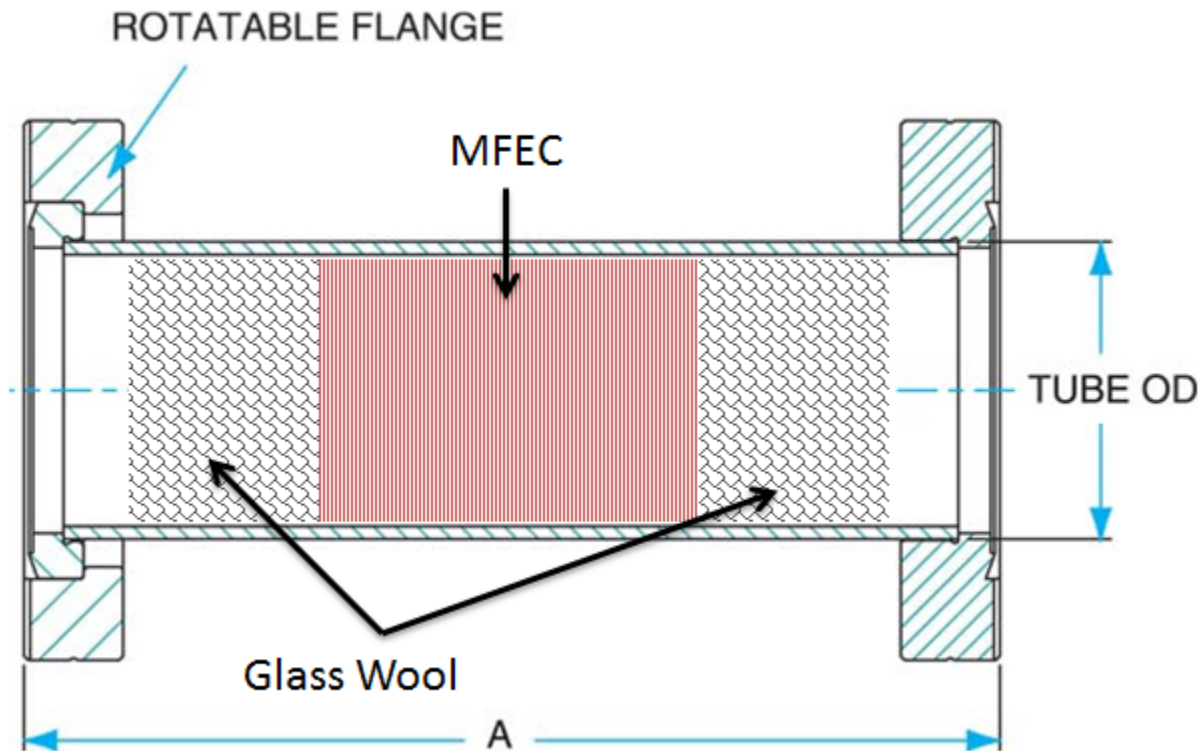
Figure 2-6 - Diagram of a 5cm long packing of MFEC with quartz wool insulating both ends.
The amount of quartz wool used is not drawn to scale.

2.3 Roughened Tube Wall Experiments

Using the techniques outlined in Section 2.2, there were two additional tubes that were

purchased to test the effect of tube "roughness" on the wall heat transfer coefficient. These tubes

were roughened using a lathe to "thread" the inside of the tube. The tool used to cut the grooves

in the wall had a 60° tip that was placed perpendicular to the tube surface during cutting. The cut

was made approximately 0.5mm deep with a varying pitch (2.36 and 7.09 threads/cm). This

increased the surface area from a baseline area of approximately 140.14 cm^2 (calculated by AC Impedance to account for surface roughness) by 13.7 and 41.6% respectively. The surface areas of the tubes were 159.34 and 198.43 cm^2. The hypothesis behind the experiment was that as the sintered metal fibers were stacked and compressed, they would expand into the grooves that were cut out. Should the fibers expand into these slots, it would allow for greater surface area in contact with the tube wall. The "smooth" tube inside can be seen in Figure 2-7 and the 7.09 thread/cm "roughened" tube inside can be seen in Figure 2-8. A schematic showing the internal geometry of the tube can be seen in Figure 2-9.

Figure 2-7 - Smooth tube wall inside view.
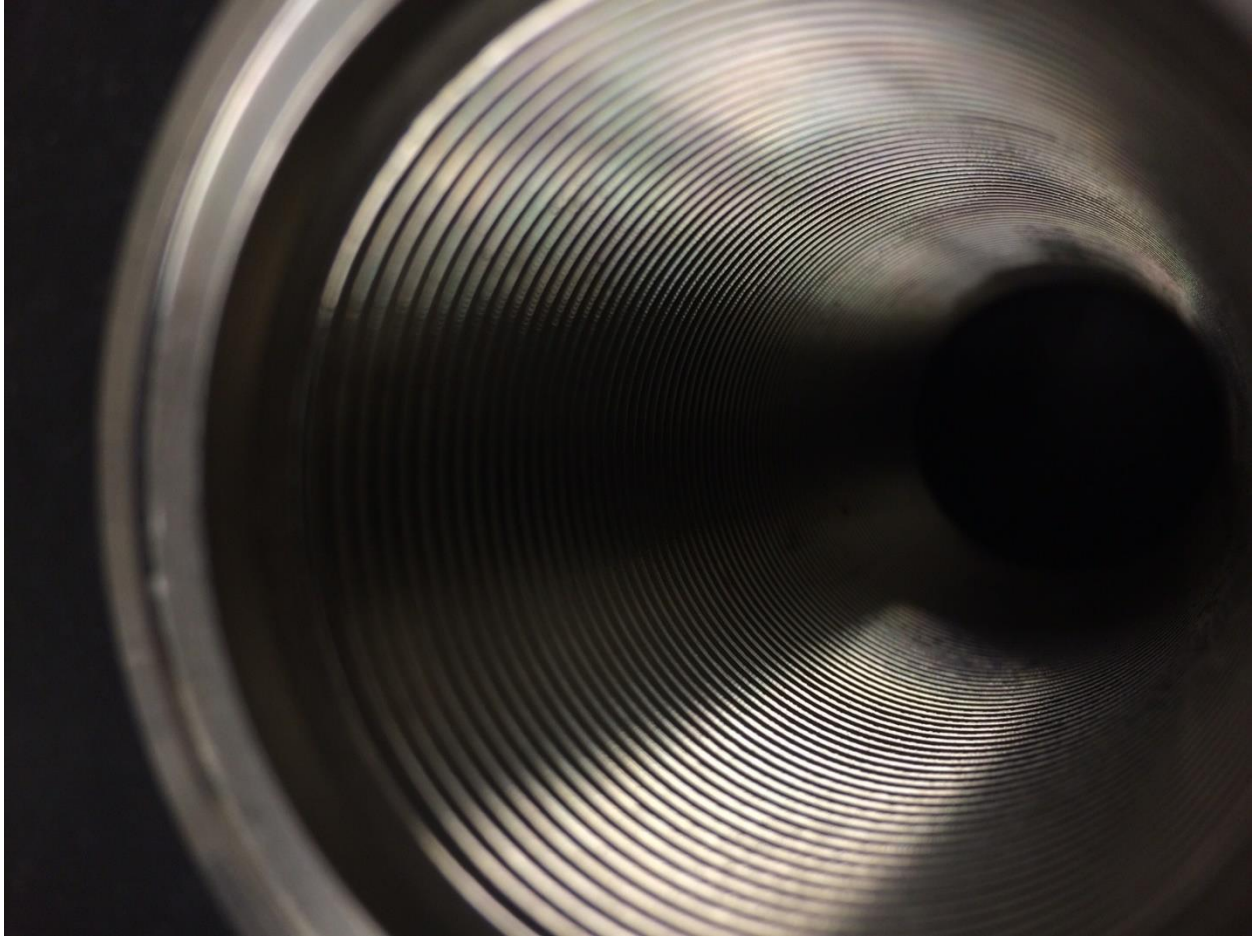
Figure 2-8 - Roughened tube wall inside view (7.09 threads/cm).
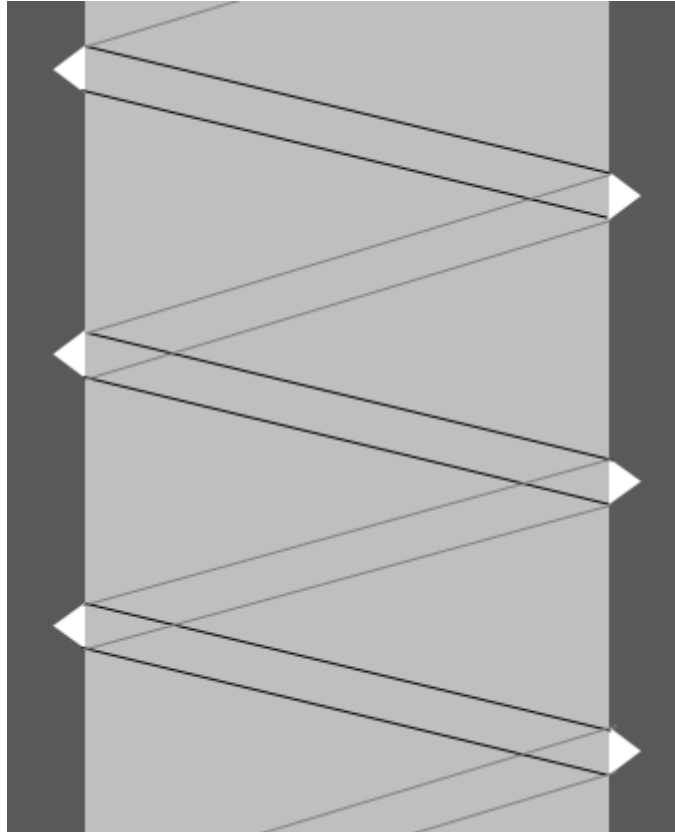
Figure 2-9 - Example of the internal geometry of a "roughened" tube. (Not drawn to scale).

2.4 Thermal Interface Material Tester

Another way to measure the contact conductance between the MFEC and the tube wall

would be to use a thermal interface material (TIM) tester. A TIM tester is simply two metal

plates that are held at fixed temperatures while a variable wattage heater is controlled by a

computer. Since the temperatures, wattage, contact pressure and surface area in contact were

known, the resistance of the material between the two plates could be accurately measured. With

this method, the contact resistances of the material could be determined if the thermal

conductivity of the material is known. When materials are run under different pressures, the

thermal conductivity of the material being tested should not change in thickness for best results in extracting thermal parameters.
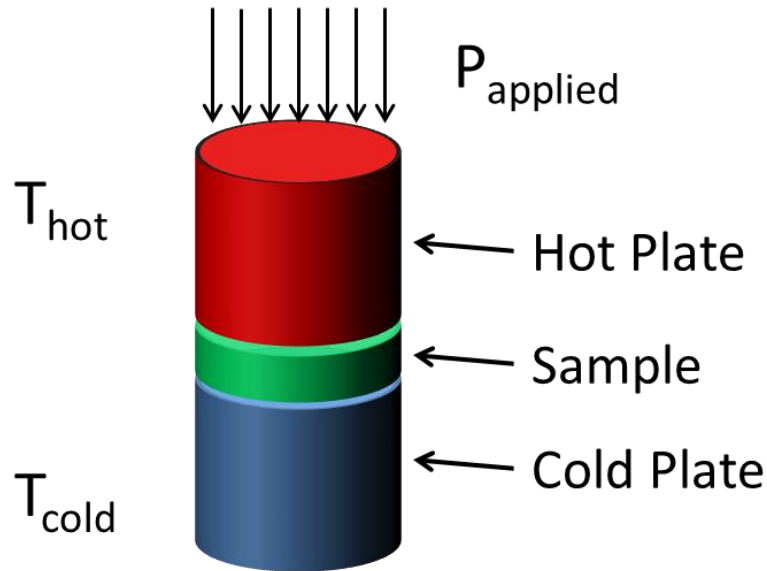
Figure 2-10 - Schematic of the principles behind TIM testing. The pressure applied to the sample is controlled while the heat flux and temperatures are measured.

The TIM tester used was a TIM Tester 1300 by Analysis Tech (Serial#1120716). It had two smooth stainless steel plates (33mm in diameter) that a pre-cut sample is placed in between. The sample was punched out using a circular punch (33mm in diameter). The TIM tester also had a variable pressure plate equipped. This allowed for the sample to be held at a range of temperatures and pressures. The temperature was set to 50°C for all of the samples run as a rough average of the average temperature of the radial conduction experiments. The pressure kit used in the experiments performed in these tests was the 5-95psi (34.5 to 655 kPa) kit (AnalysisTech).
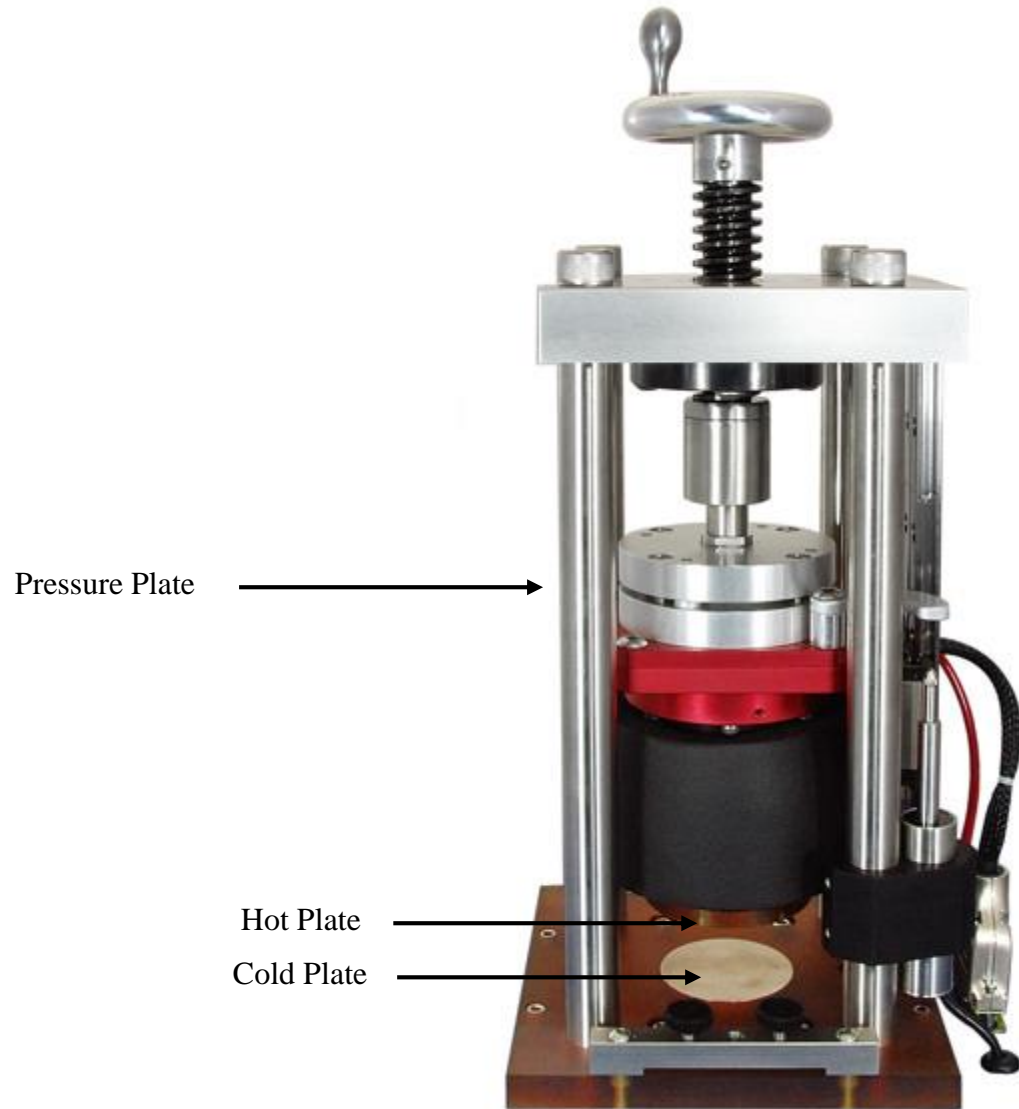
Figure 2-11- TIM Tester by Analysis Tech

2.5 Thermal Conductivity Tester by Thermal Effusivity

To further investigate the effective axial thermal conductivity, a second device was used

to test representative samples of each fiber diameter. The testing apparatus was a C-THERM TCi

Thermal Conductivity Analyzer with the T304 probe equipped. A schematic of how the apparatus functions can be seen in Figure 2-12. The device can be seen in Figure 2-13.
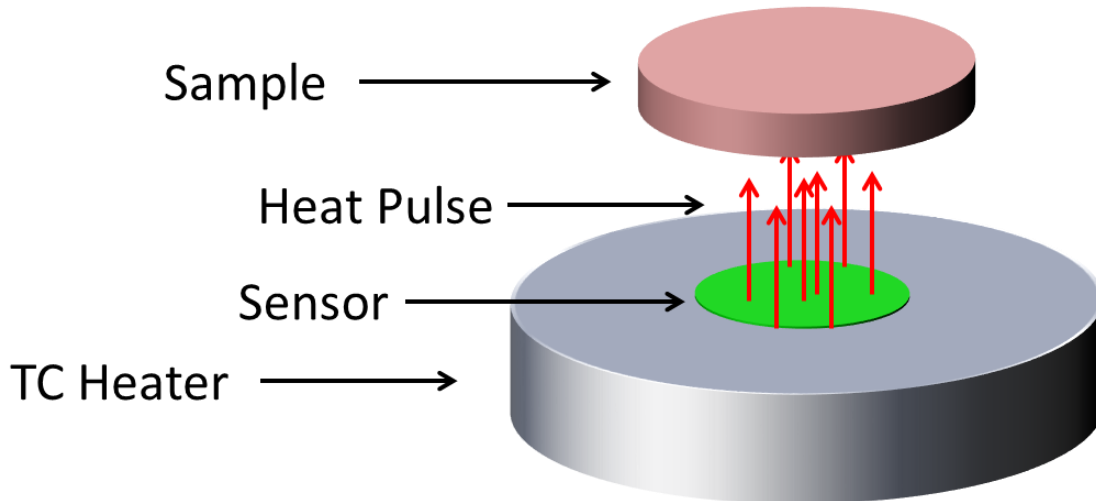
Figure 2-12 – Schematic of CTherm Thermal Conductivity Analyzer by Analysis Tech. For experimentation, sample is placed directly onto the sensor.

Figure 2-13 - CTherm Thermal Conductivity Analyzer by Analysis Tech

The device works by emitting a small pulse of heat from a resistive heater while measuring a voltage change corresponding to the amount of heat the sample absorbed. For example, if a sample were placed on the tester's surface, the device would emit a small pulse of heat that would be absorbed by the sample proportional to its thermal conductivity. This proportionality is calculated by the device by measuring the voltage drop of the sensor element. Samples with higher thermal conductivity will cause a higher drop in voltage (higher temperature drop of sensor element) than a sample with a lower thermal conductivity (lower temperature drop of sensor element). Thermal effusivity is defined in Equation (2.1).

$$e = \sqrt{k\rho c_p} \tag{2.1}$$

2.6 Hardness Testing with Nano-Indentation

As discussed in Section 1.3, an important factor in contact conductance is the hardness of the two materials in contact with each other. Since the copper fibers used to make the MFEC structure were sintered at a high temperature and allowed to slowly cool, the crystal structure of the copper was annealed in the process. Whenever a material is annealed and allowed to slowly cool, it becomes softer due to the removal of internal stresses of the structure caused by cold working (wire drawing). A nano-indenter was used to test the material properties of the fibers before and after sintering to determine the change in hardness from the annealing process. The nano-indenter used was an MTS Nanoindenter XP (Berkovich indenter tip) with Testworks software and averaging software called Analyst. A continuous stiffness method was used in the tests. The results of the tests are found in Table 2-2.

Material Tested	Hardness [GPa]	Elastic Modulus [GPa]
Bulk Copper [11]	1.350	122
12-Micron Unsintered	1.305	104
12-Micron Sintered	1.068 (18% Reduction)	127 (less elastic)

Table 2-2 - Hardness and elastic modulus of bulk copper and copper fibers before and after annealing (800°C for 45mins)

The sintering conditions and process are described and detailed in Section 1.4. All of the copper

fiber diameters are assumed to have these same properties in all of the experiments performed.

3. PROCEDURES AND RESULTS

3.1 Assumptions and Approximations

It must be stated before the following discussions all of the assumptions and approximation that were made in the experimental process. The most important assumption made that applies to all experiments is that the sintered metal fiber matrix was treated as a homogenous material combined with the fluid that occupied the space in between the fibers. The fiber density and packing varied from each individual punch made from the hand sheets. This was due to the way the hand sheets were created within the wet-lay process. This effect was minimized by attempting to optimize the wet-lay process by changing the fiber-to-cellulose ratio as well as blending time. The best combination was chosen by visual inspection of the hand-sheet. If the hand-sheet had a high degree of uniformity (flatness) and "fluffiness" (the relative thickness of the sheet compared to the amount of fiber used), the sheet was considered "acceptable" to use for experimentation.

Since the density of each sheet is variable, it was difficult to calculate the amount of pressure to apply to the sheet to obtain a certain metal volume percent. Also, the metal volume percentage varied with the fiber diameter as well. Therefore in the results, the reported metal volume percent is considered a "bulk" value and does not necessarily represent a local metal volume percent where the measurements are occurring. The assumption in these experiments are that the metal volume percent is constant throughout the material being tested.

For the radial temperature measurements, the placement and accuracy of the thermocouples was extremely important to ensure that the correct parameters would be extracted from the temperature data. During the experimentation it was assumed that the thermocouples were placed accurately and did not shift from the position they were placed in. The

thermocouple holder also contributed to the radial heat transfer, but was assumed to be negligible. The end effects from the tube and MFEC were considered to be negligible in this study as well.

The water bath was assumed to be well-mixed, turbulent and at a uniform temperature. The bath was vigorously stirred and the thermal mass of the water was considerably higher than the thermal mass of the experimental apparatus. This was confirmed when the temperature of the water bath only decreased by 1-2°C after the tube was submerged into the water bath. Another assumption was that the temperature of the outer wall and the temperature of the water bath were identical. This assumption was based on a near-infinite heat transfer coefficient on the outside of the wall to make the radial conduction analysis simpler and more consistent.

For all simulation and mathematical analysis, lumped/bulk heat transfer properties were used. These properties will be referred to as "effective" heat transfer properties. Equations (3.1) and (3.2) show how the bulk material properties are calculated.

$$\rho = \chi_{\text{fibers}}\rho_{\text{fibers}} + \chi_{\text{fluid}}\rho_{\text{fluid}} \tag{3.1}$$

$$c_p = \varphi_{\text{fibers}}c_{p_{\text{fibers}}} + \varphi_{\text{fluid}}c_{p_{\text{fluid}}} \tag{3.2}$$

where χ is the mass fraction φ is the volume fraction of each component of the MFEC.

3.2 Radial Temperature Tests

For the radial temperature tests, the effects of fiber diameter on the wall heat transfer coefficient were tested using 6, 12 and 25 micron fibers. The fibers were packed into the tube at an identical volume percent (8.8 to 8.9 vol%). The fibers were tested under rough vacuum and

with various gases replacing the interstitial volume between the fibers. The raw temperature data

from a test of 12 micron fibers with Helium as the interstitial fluid can be seen in Figure 3-1.
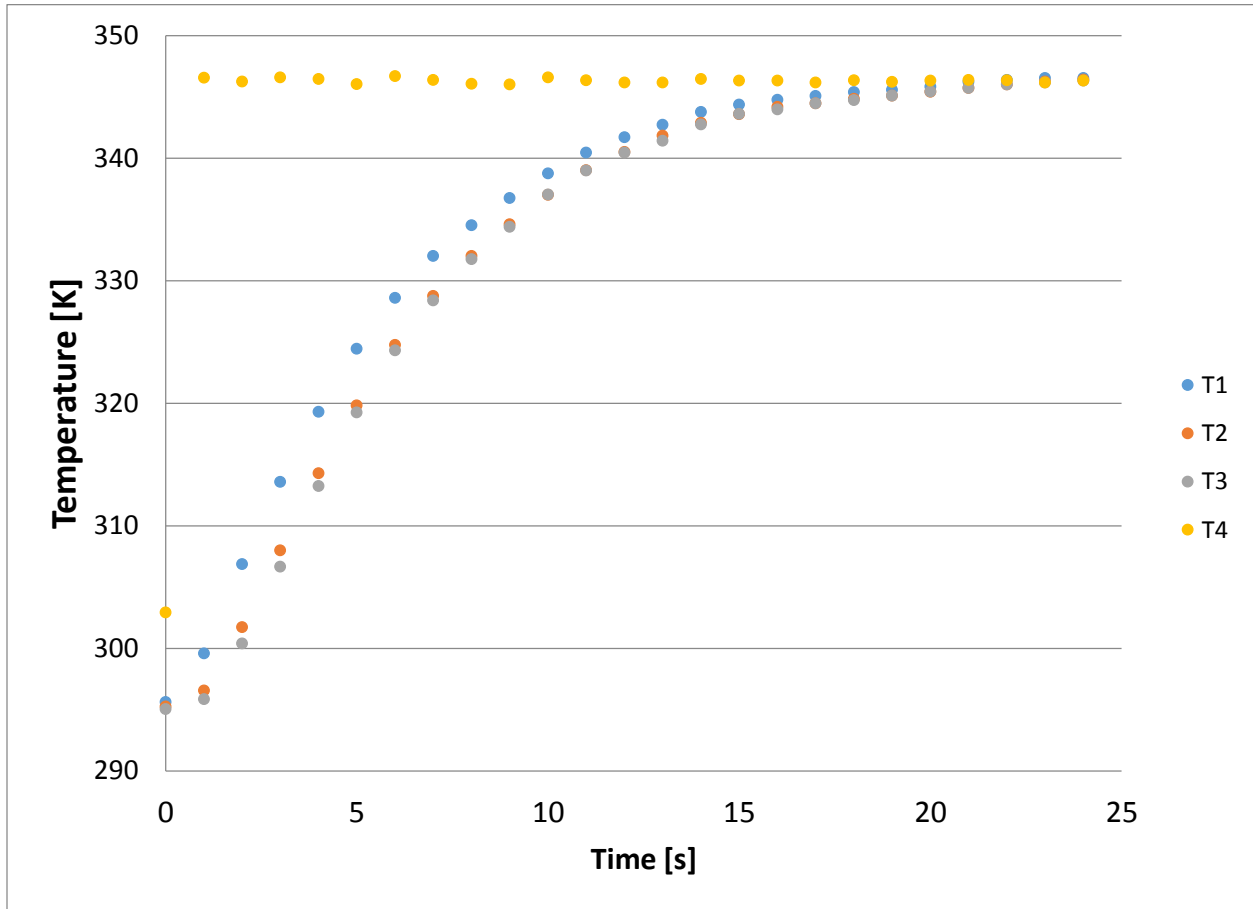
Figure 3-1- Raw Temperature data from helium test with 12 micron fibers (See Figure 2-5 for thermocouple location)

3.3 Transient Heat Transfer Analysis and Results

In order for this temperature data to be interpreted into effective thermal parameters, a

transient heat transfer analysis must be used. By this method, the thermal parameters were fitted

to the temperature data by a least squares error analysis using a Newton-Rhapson search

31

algorithm.   The model was derived below. A schematic of the model domain is shown in
Figure 3-2.
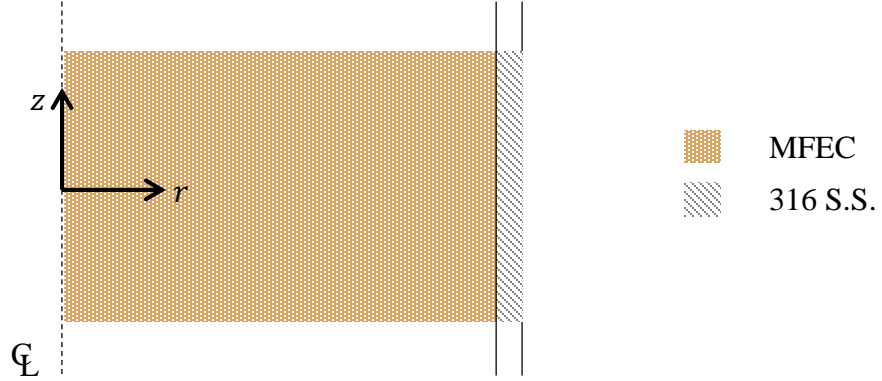
Figure 3-2 - Schematic of transient heat transfer model domain. (Not to scale)

One-dimensional radial transient heat transfer by conduction is defined in Eq. (3.3):

$$\rho c_p \frac{\partial T}{\partial t} = \frac{1}{r}\frac{\partial}{\partial r}\left(kr\frac{\partial T}{\partial r}\right) \tag{3.3}$$

Assuming the density, thermal conductivity, specific heat, time step and grid spacing remain

constant, Eq. (3.3) can be drastically simplified. Discretizing Eq. (3.3) using a forward-time

centered-space differencing scheme (also known as the Euler Implicit Method) gives Eq. (3.4):

$$\rho c_p \frac{T_i^{l+1} - T_i^l}{\Delta t} = \frac{1}{r_i \Delta r}\left[\left(kr_{i+1/2}\frac{T_{i+1}^{l+1} - T_i^{l+1}}{\Delta r}\right) - \left(kr_{i-1/2}\frac{T_i^{l+1} - T_{i-1}^{l+1}}{\Delta r}\right)\right] \tag{3.4}$$

Rearranging and consolidating like-terms, Eq. (3.4) can be represented in Eq. (3.5):

$$T_i^{l+1} - T_i^l = \left(\frac{k}{\rho c_p}\right)\left(\frac{\Delta t}{\Delta r^2}\right)\left[\left(\frac{r_{i+1/2}}{r_i}\right)\left(T_{i+1}^{l+1} - T_i^{l+1}\right) - \left(\frac{r_{i-1/2}}{r_i}\right)\left(T_i^{l+1} - T_{i-1}^{l+1}\right)\right]$$

$$\alpha = \left(\frac{k}{\rho c_p}\right), \quad \text{Fo} = \left(\frac{\alpha \Delta t}{\Delta r^2}\right)$$

$$T_i^{l+1} - T_i^l = \text{Fo}\left[\left(\frac{r_{i+1/2}}{r_i}\right)\left(T_{i+1}^{l+1} - T_i^{l+1}\right) - \left(\frac{r_{i-1/2}}{r_i}\right)\left(T_i^{l+1} - T_{i-1}^{l+1}\right)\right]$$

$$T_i^l = -\left(\text{Fo}\frac{r_{i+1/2}}{r_i}\right)T_{i+1}^{l+1} + \left[\left(\text{Fo}\frac{r_{i+1/2}}{r_i}\right) + \left(\text{Fo}\frac{r_{i-1/2}}{r_i}\right) + 1\right]T_i^{l+1} - \left(\text{Fo}\frac{r_{i-1/2}}{r_i}\right)T_{i-1}^{l+1} \quad (3.5)$$

The centerline symmetry boundary at $r = 0$ is defined in Eq. (3.6) [23]:

$$\lim_{r \to 0}\frac{1}{r}\frac{\partial}{\partial r}\left(kr\frac{\partial T}{\partial r}\right) = k\frac{\partial^2 T}{\partial r^2} \approx 2k\frac{T_2^{l+1} - T_1^{l+1}}{\Delta r^2}$$

$$\frac{\rho c_p}{2}\frac{T_1^{l+1} - T_1^l}{\Delta t} = 2k\frac{T_2^{l+1} - T_1^{l+1}}{\Delta r^2}$$

$$T_1^{l+1} - T_1^l = 4\left(\frac{k}{\rho c_p}\right)\left(\frac{\Delta t}{\Delta r^2}\right)\left(T_2^{l+1} - T_1^{l+1}\right)$$

$$T_1^{l+1} - T_1^l = 4\text{Fo}\left(T_2^{l+1} - T_1^{l+1}\right)$$

$$T_1^l = -4\text{Fo}T_2^{l+1} + (4\text{Fo} + 1)T_1^{l+1} \quad (3.6)$$

The convective boundary at the surface of the stainless steel wall is defined in Eq. (3.7):

$$\frac{\rho c_p}{2}\frac{T_i^{l+1} - T_i^l}{\Delta t} = \frac{1}{r_i \Delta r}\left[h\left(T_\infty^{l+1} - T_i^{l+1}\right) - \left(kr_{i-1/2}\frac{T_i^{l+1} - T_{i-1}^{l+1}}{\Delta r}\right)\right]$$

$$T_i^{l+1} - T_i^l = \left(\frac{h}{\rho c_p}\right)\left(\frac{1}{r_n}\right)\frac{2\Delta t}{\Delta r}\left(T_\infty^{l+1} - T_i^{l+1}\right) - \left(\frac{k}{\rho c_p}\right)\left(\frac{2\Delta t}{\Delta r^2}\right)\left(\frac{r_{i-1/2}}{r_i}\right)\left(T_i^{l+1} - T_{i-1}^{l+1}\right)$$

$$T_i^{l+1} - T_i^l = -2\text{Fo}\left[\left(\frac{r_{i-1/2}}{r_i}\right)\left(T_i^{l+1} - T_{i-1}^{l+1}\right)\right] + \left(\frac{h}{\rho c_p}\right)\left(\frac{1}{r_n}\right)\frac{2\Delta t}{\Delta r}\left(T_\infty^{l+1} - T_i^{l+1}\right)$$

$$T_i^l + \left(\frac{h}{\rho c_p}\right)\left(\frac{1}{r_n}\right)\frac{2\Delta t}{\Delta r}T_\infty^{l+1}$$

$$= \left[2\text{Fo}\left(\frac{r_{i-1/2}}{r_i}\right) + \left(\frac{h}{\rho c_p}\right)\left(\frac{1}{r_n}\right)\left(\frac{2\Delta t}{\Delta r}\right) + 1\right]T_i^{l+1} - 2\text{Fo}\left(\frac{r_{i-1/2}}{r_i}\right)T_{i-1}^{l+1}$$

(3.7)

The contact resistance between the MFEC and the stainless steel wall is modeled by two super-imposed node points. One node point is used to represent the temperature of the MFEC at the contact and the other is used to represent the temperature of the stainless steel wall at the contact point. Figure 3-3 visualizes the node system at the contact point.

$$n - 2 \qquad n - 1 \qquad n_{MFEC} \qquad n + 1 \qquad n + 2$$

$$n_{SS}$$
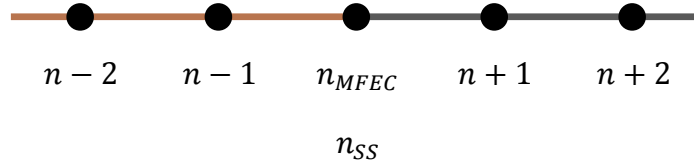
Figure 3-3 - Node System for Contact Interface

The contact resistance, h_{wall}, is defined in Eqs. (3.8) and (3.9):

$$\frac{\rho c_p \Delta r}{2}\frac{T_i^{l+1} - T_i^l}{\Delta t} = k\left(\frac{r_{n\_SS+1/2}}{r_{n\_SS}}\right)\left(\frac{T_{n+1}^{l+1} - T_{n\_SS}^{l+1}}{\Delta r}\right) + h_{\text{wall}}\left(\frac{1}{r_{n\_SS}}\right)\left(T_{n\_MFEC}^{l+1} - T_{n\_SS}^{l+1}\right)$$

$$T_{n\_SS}^{l+1} - T_{n\_SS}^l = \left(\frac{k}{\rho c_p}\right)\left(\frac{2\Delta t}{\Delta r^2}\right)\left(\frac{r_{n\_SS+1/2}}{r_{n\_SS}}\right)\left(T_{n+1}^{l+1} - T_{n\_SS}^{l+1}\right)$$

$$+ \left(\frac{h_{\text{wall}}}{\rho c_p}\right)\left(\frac{1}{r_{n\_SS}}\right)\left(\frac{2\Delta t}{\Delta r}\right)\left(T_{n\_MFEC}^{l+1} - T_{n\_SS}^{l+1}\right)$$

$$T_{n\_SS}^{l+1} - T_{n_{SS}}^{l} = 2\text{Fo}\left(\frac{r_{n\_SS+1/2}}{r_{n\_SS}}\right)\left(T_{n+1}^{l+1} - T_{n\_SS}^{l+1}\right)$$

$$+ \left(\frac{h_{\text{wall}}}{\rho c_p}\right)\left(\frac{1}{r_{n\_SS}}\right)\left(\frac{2\Delta t}{\Delta r}\right)\left(T_{n\_MFEC}^{l+1} - T_{n\_SS}^{l+1}\right)$$

$$T_{n_{SS}}^{l} = -\left(\frac{h_{\text{wall}}}{\rho c_p}\right)\left(\frac{2\Delta t}{\Delta r}\right)T_{n\_MFEC}^{l+1} + \left[2\text{Fo}\left(\frac{r_{n\_SS+1/2}}{r_{n\_SS}}\right) + \left(\frac{h_{\text{wall}}}{\rho c_p}\right)\left(\frac{2\Delta t}{\Delta r}\right) + 1\right]T_{n\_SS}^{l+1}$$

$$- 2\text{Fo}\left(\frac{r_{n\_SS+1/2}}{r_{n\_SS}}\right)T_{n+1}^{l+1}$$

(3.8)

$$T_{n\_MFEC}^{l} = -2\text{Fo}\left(\frac{r_{n\_SS-1/2}}{r_{n\_SS}}\right)T_{n-1}^{l+1} + \left[2\text{Fo}\left(\frac{r_{n_{SS}-1/2}}{r_{n\_SS}}\right) + \left(\frac{h_{\text{wall}}}{\rho c_p}\right)\left(\frac{2\Delta t}{\Delta r}\right) + 1\right]T_{n\_MFEC}^{l+1}$$

$$- \left(\frac{h_{\text{wall}}}{\rho c_p}\right)\left(\frac{2\Delta t}{\Delta r}\right)T_{n\_SS}^{l+1}$$

(3.9)

Using the derived one-dimensional heat transfer model above, the temperature data was fitted to obtain the best-fit parameters for k_{eff} and h_{wall}. While these parameters might not be the exact values for the material being tested, they represent the ideal behavior of the experiment carried out under the set initial conditions. The results of the tests can be seen in Table 3-1, Table 3-2, Figure 3-4, Figure 3-5, Figure 3-6, Figure 3-7, Figure 3-8 and Figure 3-9.

	k_{eff} [W·m⁻¹·K⁻¹]		
Interstitial Fluid	**6 Micron**	**12 Micron**	**25 Micron**
Rough Vacuum (<500 torr)	3.18 ± 0.15	3.66 ± 0.16	3.35 ± 0.05
Krypton	3.15 ± 0.16	3.79 ± 0.10	3.17 ± 0.10
Argon	3.47 ± 0.36	4.58 ± 0.18	4.27 ± 0.23
Nitrogen	3.70 ± 0.13	4.99 ± 0.21	4.09 ± 0.14
Neon	4.13 ± 0.29	5.45 ± 0.36	5.41 ± 0.24
Helium	4.97 ± 0.26	6.62 ± 0.14	6.80 ± 0.31
Hydrogen	5.53 ± 0.24	n/a	6.80 ± 0.26

Table 3-1 - Effective thermal conductivity of MFEC using various interstitial fluids. Tested under stagnant (no gas flow) conditions, 8.8 vol% fibers, smooth tube wall, 1 atm pressure for each gas.

	h_{wall} [W·m⁻²·K⁻¹]		
Interstitial Fluid	**6 Micron**	**12 Micron**	**25 Micron**
Rough Vacuum (<500 torr)	856 ± 34	1067 ± 44	712 ± 22
Krypton	742 ± 22	1194 ± 71	771 ± 24
Argon	822 ± 61	1448 ± 49	1042 ± 35
Nitrogen	1053 ± 72	1652 ± 31	1069 ± 36
Neon	1283 ± 65	1850 ± 153	1698 ± 79
Helium	2105 ± 175	2378 ± 81	2939 ± 339
Hydrogen	2573 ± 434	n/a	2337 ± 169

Table 3-2 – Wall heat transfer coefficients of MFEC using various interstitial fluids. Tested under stagnant (no gas flow) conditions, 8.8 vol% fibers, smooth tube wall, 1 atm pressure for each gas
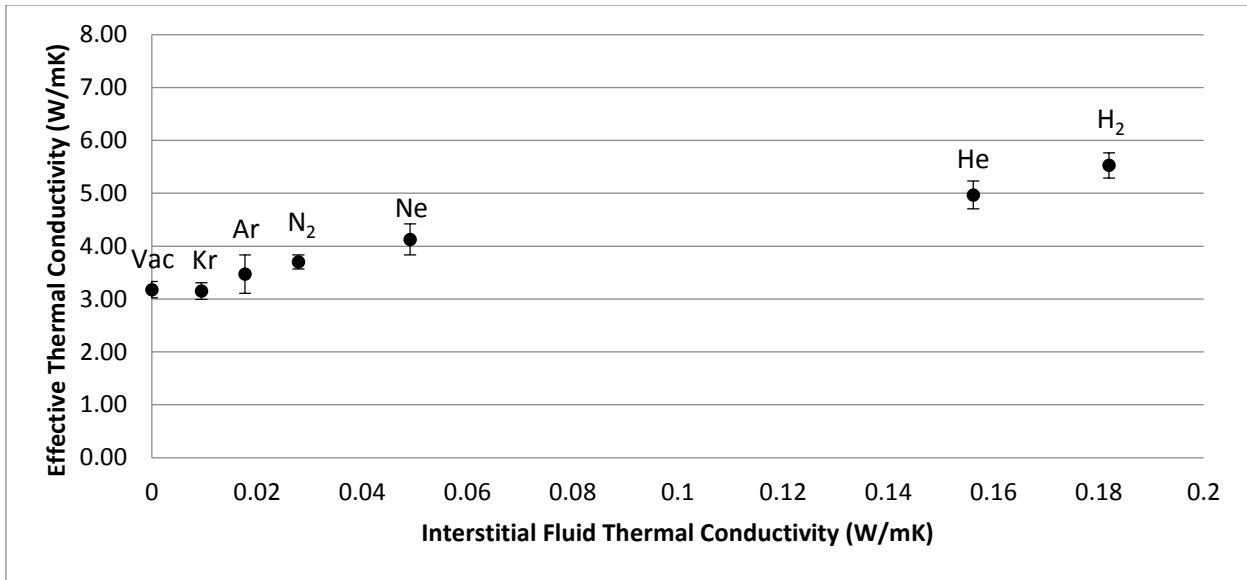
Figure 3-4 - Effective Thermal Conductivity for 6 Micron Fiber Tests. Tested under stagnant (no gas flow) conditions, 8.8 vol% fibers, smooth tube wall, 1 atm pressure for each gas except for vacuum. Vacuum thermal conductivity was represented as 0 [$Wm^{-1}K^{-1}$].
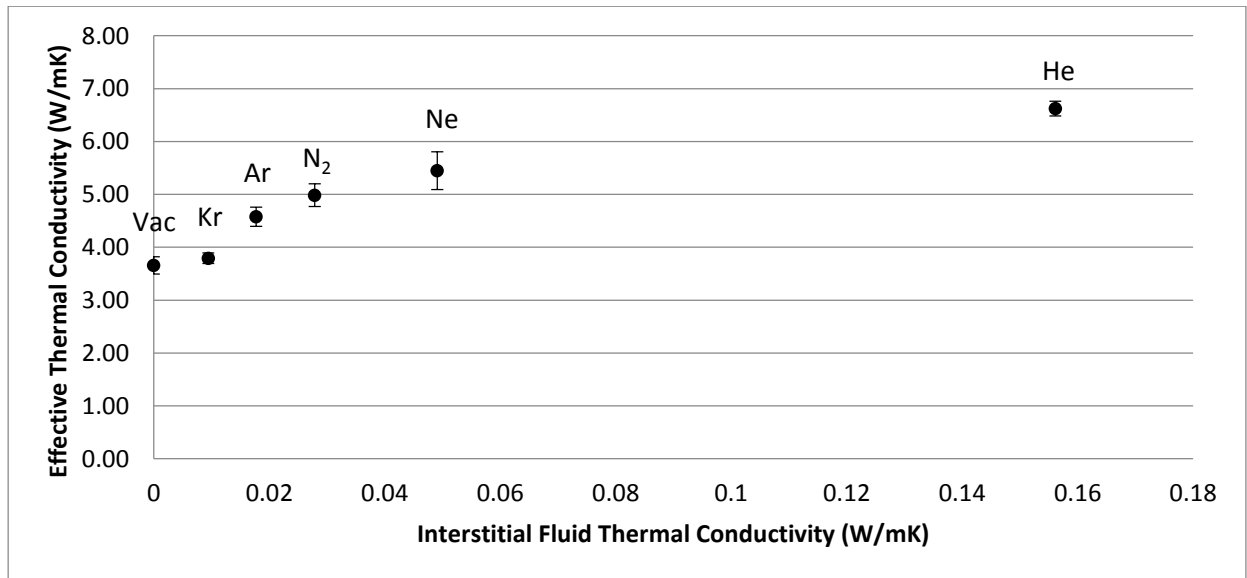
Figure 3-5 - Effective Thermal Conductivity for 12 Micron Fiber Tests. Tested under stagnant (no gas flow) conditions, 8.8 vol% fibers, smooth tube wall, 1 atm pressure for each gas except for vacuum. Vacuum thermal conductivity was represented as 0 [$Wm^{-1}K^{-1}$].
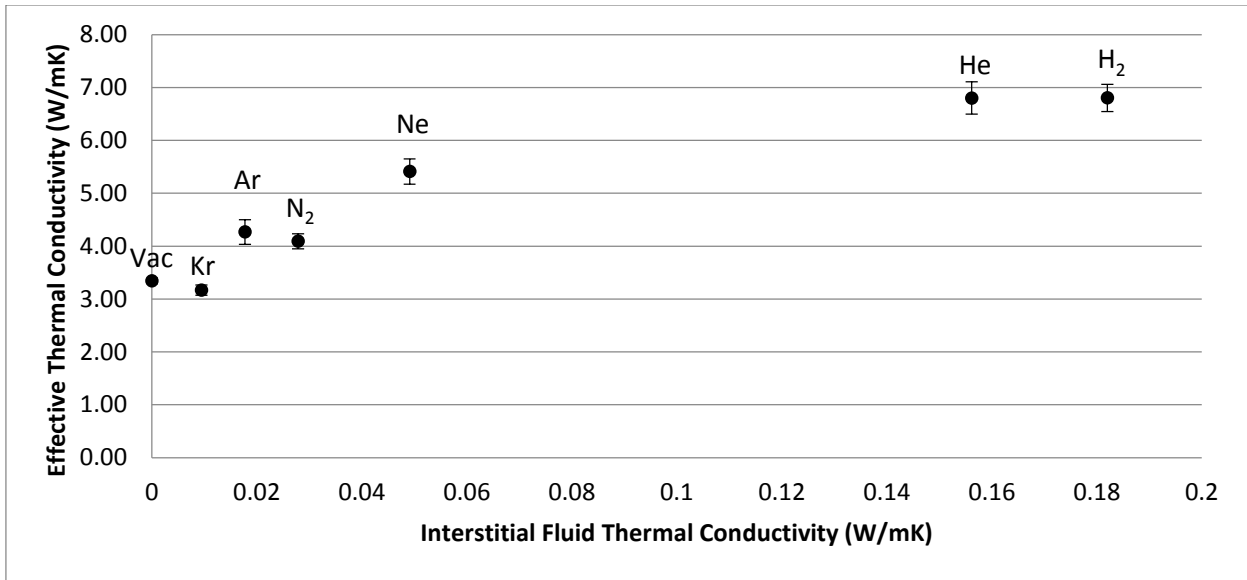
Figure 3-6 -Effective Thermal Conductivity for 25 Micron Fiber Tests. Tested under stagnant (no gas flow) conditions, 8.8 vol% fibers, smooth tube wall, 1 atm pressure for each gas except for vacuum. Vacuum thermal conductivity was represented as 0 [$Wm^{-1}K^{-1}$].
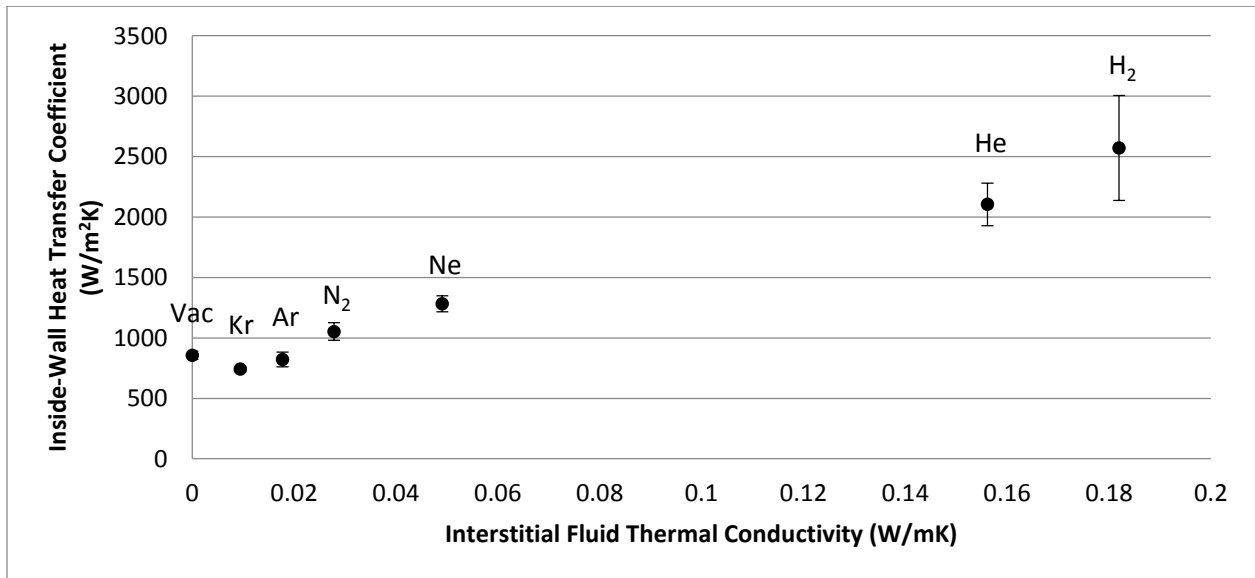
Figure 3-7 - Inside-Wall Heat Transfer Coefficients for 6 Micron Tests. Tested under stagnant (no gas flow) conditions, 8.8 vol% fibers, smooth tube wall, 1 atm pressure for each gas except for vacuum. Vacuum thermal conductivity was represented as 0 [$Wm^{-1}K^{-1}$].
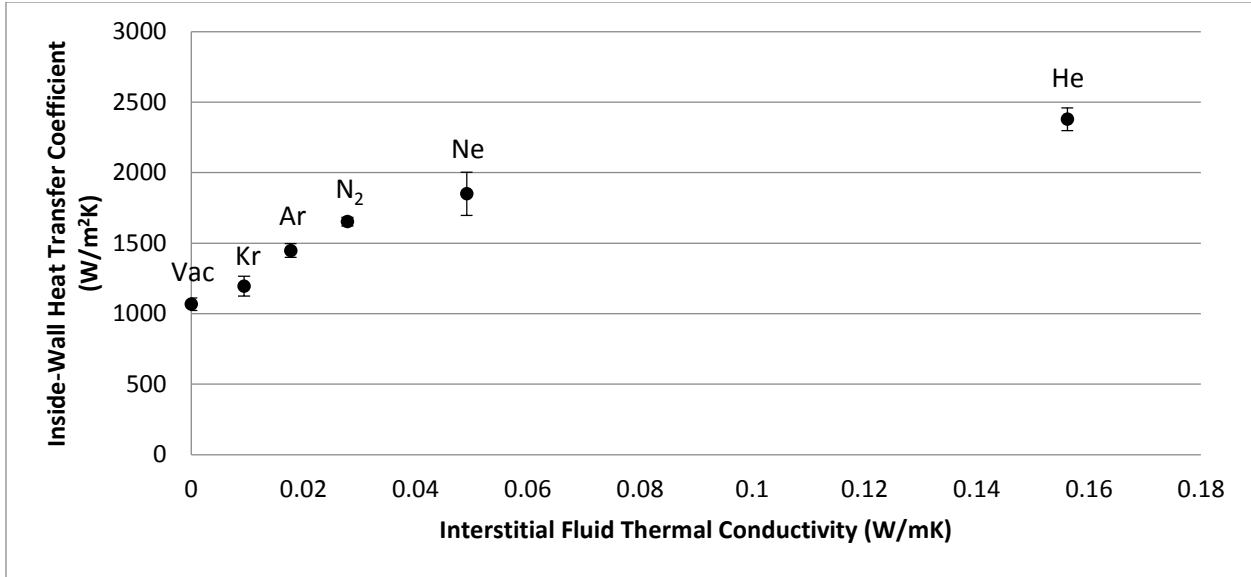
Figure 3-8 - Inside-Wall Heat Transfer Coefficients for 12 Micron Tests. Tested under stagnant (no gas flow) conditions, 8.8 vol% fibers, smooth tube wall, 1 atm pressure for each gas except for vacuum. Vacuum thermal conductivity was represented as 0 [$Wm^{-1}K^{-1}$].
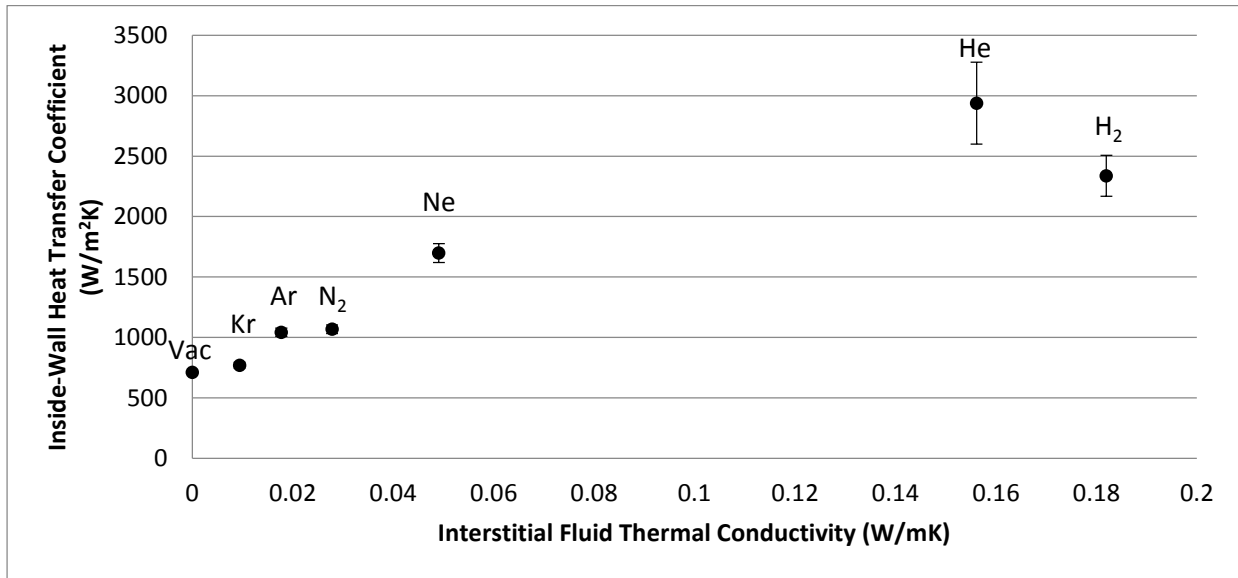
Figure 3-9 - Inside- Wall Heat Transfer Coefficients for 25 Micron Tests. Tested under stagnant (no gas flow) conditions, 8.8 vol% fibers, smooth tube wall, 1 atm pressure for each gas except for vacuum. Vacuum thermal conductivity was represented as 0 [$Wm^{-1}K^{-1}$].

Best fit equations for the modeling of the thermal conductivity can be found in Table 3-3 and Table 3-4. These equations are valid over the specified range of values and should only be used to predict gas-phase interstitial fluids. Since the wall heat transfer coefficient also follows a logarithmic trend, the value of 0 is not included in the specified range. Also it is worth noting that these equations are valid for a copper metal vol% of approximately 8.8%.

	k_{eff} [W·m^{-1}·K^{-1}]	Specified Range for k_g
6 Micron	$= 0.7602ln(k_g) + 6.5458$	9.4E-3 to 0.182
12 Micron	$= 0.9849ln(k_g) + 8.4642$	9.4E-3 to 0.182
25 Micron	$= 1.2505ln(k_g) + 9.0196$	9.4E-3 to 0.182

Table 3-3 - Fitted equations for effective thermal conductivity as a function of interstitial fluid thermal conductivity

	h_{wall} [W·m^{-2}·K^{-1}]	Specified Range for k_g
6 Micron	$= 603.4ln(k_g) + 3325.5$	9.4E-3 to 0.182
12 Micron	$= 419.82ln(k_g) + 3144.5$	9.4E-3 to 0.182
25 Micron	$= 679.92ln(k_g) + 3778.9$	9.4E-3 to 0.182

Table 3-4 - Fitted equations for wall heat transfer coefficient as a function of interstitial fluid thermal conductivity

These results will be discussed further in Section 4.1.

3.4 Roughened Tube Wall Experimental Results

The roughened tubes were packed and tested exactly the same as the smooth tube walls. The thermal conductivity was set for all tests as a constant value for all three tubes to test the effect on the wall heat transfer coefficient. For simplicity, only vacuum and nitrogen were used these tests. The thermal conductivity of the MFEC in vacuum was set at 3.42 [W·m^{-1}·K^{-1}] and nitrogen was set at 3.79 [W·m^{-1}·K^{-1}]. In these results, the smooth tube wall will be the result obtained in Section 3.3. The results are seen in Table 3-5 and Figure 3-10.

	k_{eff} [W·m^{-1}·K^{-1}]		
Interstitial Fluid	**Smooth**	**13.9% Rough**	**41.6% Rough**
Rough Vacuum (<500 torr)	1067 ± 44	453 ± 20	492 ± 18
Nitrogen	1652 ± 31	631 ± 41	645 ± 10

Table 3-5 – Wall Heat Transfer Coefficient vs. Tube Roughness. Tested under stagnant (no gas flow) conditions, 8.8 vol% fibers, 1 atm pressure for each gas except for vacuum. Vacuum thermal conductivity was represented as 0 [Wm^{-1}K^{-1}].
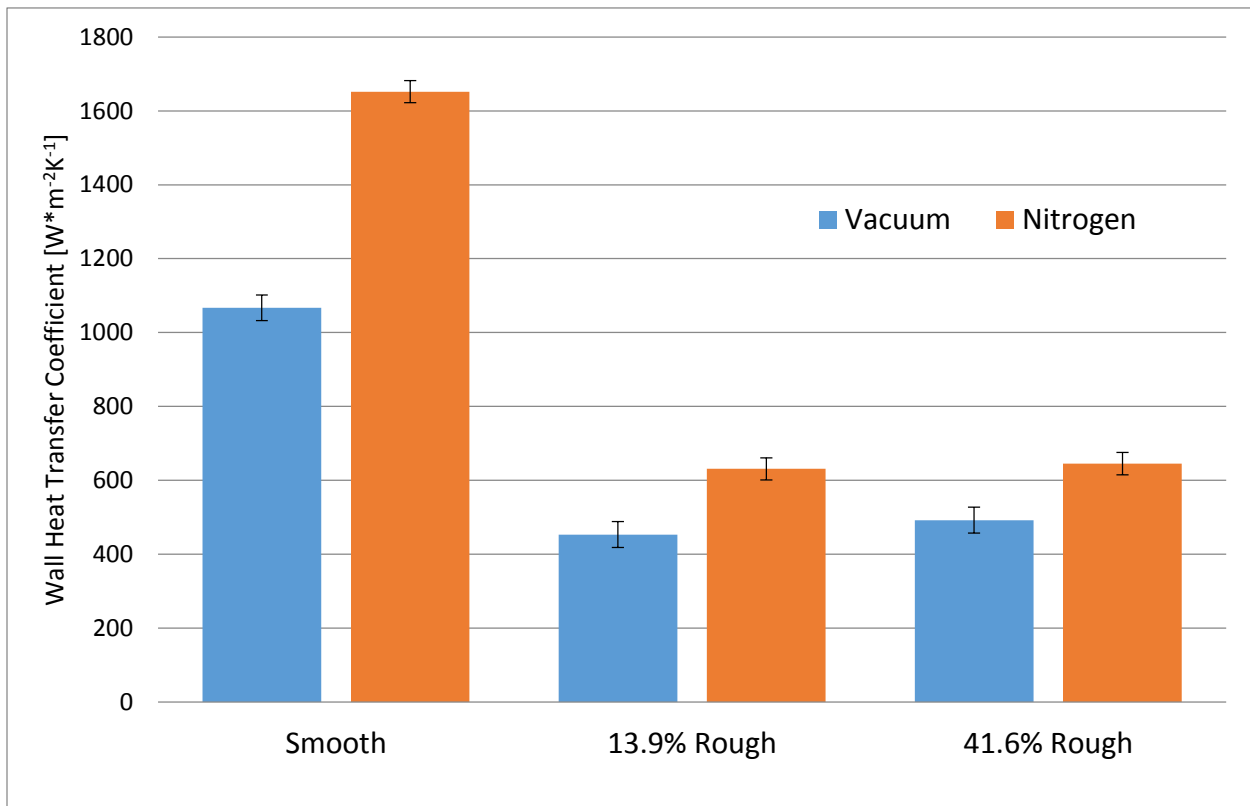
Figure 3-10 - Wall Heat Transfer Coefficient for Roughened Tubes. Tested under stagnant (no gas flow) conditions, 8.8 vol% fibers, 1 atm pressure for Nitrogen tests.

These results will be discussed further in Section 4.2.

3.5 Flowing Gas Experiments

Using the experimental apparatus described in Section 2.2, the MFEC was tested under flowing gas conditions. A slight addition to the apparatus includes the removal of the radial thermocouples and inserting two fine-wire thermocouples at the entrance and exit of the tube. These thermocouples will measure the inlet and outlet gas bulk temperatures. Since the flow will be turbulent (Re > 2000), the flow is assumed to be well mixed and at a uniform temperature. The water bath temperature (T_∞) was recorded and was assumed to be the wall temperature (T_w). The flowing gas will be compressed nitrogen at approximately 3 atm. The MFEC bed was approximately 2.6 cm long for each fiber blend packed to an approximate density of 8.0 vol%. The temperature data collected at various flow rates can be seen in Table 3-6, Table 3-7 and Table 3-8.

Velocity [m/s]	Flow Rate [L/min]	T_inlet [°C]	T_outlet [°C]	T_inf [°C]
0.07	3	35.0	54.0	83.6
0.09	4	35.0	57.5	83.5
0.11	5	35.0	60.1	83.6
0.13	6	35.0	63.9	82.9
0.15	7	35.0	66.8	82.6
0.18	8	35.0	69.6	82.3
0.20	9	35.0	71.3	81.6
0.22	10	35.0	72.6	81.8
0.24	11	35.0	73.1	81.3
0.26	12	35.0	73.6	81.4

Table 3-6 - Temperature data from flowing gas experiments. 6 micron fibers, 2.6cm bed, flowing with N_2 gas at 3atm.

Velocity [m/s]	Flow Rate [L/min]	T_inlet [°C]	T_outlet [°C]	T_inf [°C]
0.07	3	30.0	47.8	72.1
0.09	4	30.0	52.7	72.6
0.11	5	30.0	55.8	72.7
0.13	6	30.0	59.4	73.1
0.15	7	30.0	62.0	73.4
0.18	8	30.0	64.0	73.5
0.20	9	30.0	65.8	73.8
0.22	10	30.0	67.2	74.0
0.24	11	30.0	68.4	74.3
0.26	12	30.0	68.7	74.5

Table 3-7 - Temperature data from flowing gas experiments. 12 micron fibers, 2.6cm bed, flowing with N_2 gas at 3atm.

Velocity [m/s]	Flow Rate [L/min]	T_inlet [°C]	T_outlet [°C]	T_inf [°C]
0.07	3	32.0	49.2	76.5
0.09	4	32.0	52.6	77.1
0.11	5	32.0	56.0	77.0
0.13	6	32.0	61.2	77.1
0.15	7	32.0	63.3	77.0
0.18	8	32.0	66.2	77.0
0.20	9	32.0	68.4	77.6
0.22	10	32.0	68.9	77.3
0.24	11	32.0	69.8	77.8
0.26	12	32.0	70.1	78.0

Table 3-8 - Temperature data from flowing gas experiments. 25 micron fibers, 2.6cm bed, flowing with N_2 gas at 3atm.

As a control data set for the tests, a blank tube with a smooth wall was tested under identical

flow rates. The temperature data for that test can be seen in Table 3-9.

Velocity [m/s]	Flow Rate [L/min]	T_inlet [°C]	T_outlet [°C]	T_inf [°C]

0.11	5	31.1	62.5	76.0
0.22	10	29.4	57.7	76.0
0.33	15	28.0	56.6	76.1
0.45	20	27.0	55.0	76.3
0.56	25	27.6	53.5	76.9
1.13	50	27.0	51.0	77.4

Table 3-9 - Temperature data from flowing gas experiments. Smooth tube, flowing with N2 gas at 3atm.

Using a simple calculation of the amount of heat transferred from the MFEC to the nitrogen gas, the approximate heat transfer coefficient can be calculated based on the following equations.

$$\dot{q} = \dot{m}c_p(T_{outlet} - T_{inlet}) \qquad (3.10)$$

$$\dot{q} = hA(T_\infty - T_m) \qquad (3.11)$$

In Equation (3.11), the mean temperature (T_m) is calculated based on the average temperature of the inlet and outlet gases. The internal heat transfer coefficient was calculated and plotted in Figure 3-11.
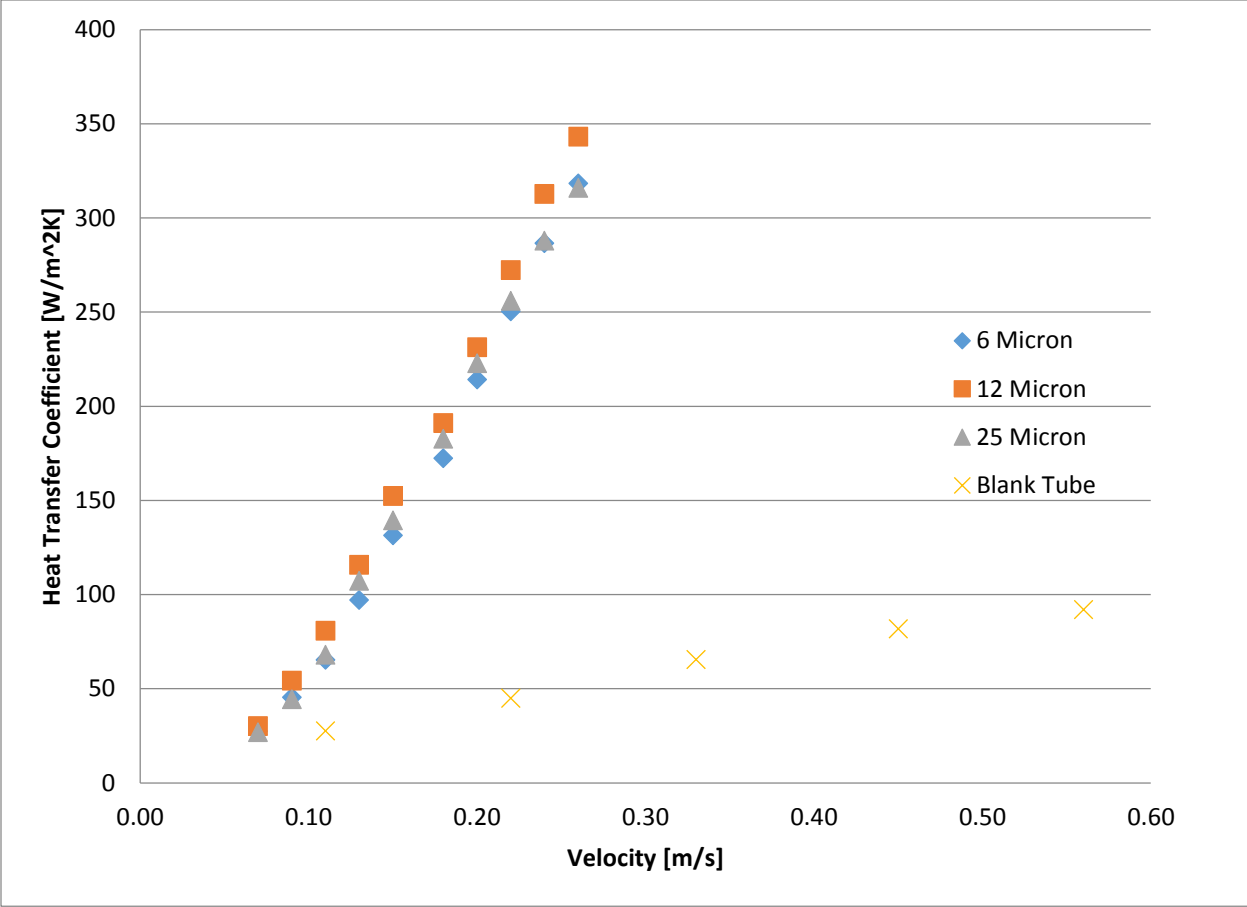
Figure 3-11 - Heat transfer coefficient vs. free stream velocity for flowing gas experiments. These results will be discussed further in Section 4.3.

3.6 Thermal Interface Material Tester Results

The first test that was run on the TIM tester was to determine if the MFEC would be an appropriate candidate for testing. As mentioned in Section 2.4, the material tested needs to maintain a relatively constant thermal conductivity with varying pressures. Since the MFEC was a deformable structure that will create additional thermal contacts as pressure is applied, it did not seem that the MFEC would be a good candidate for this testing method. To test this hypothesis, the MFEC was tested at a constant pressure with varying thickness. For example, a 25 micron sample was selected and tested under 69kPa of pressure. After obtaining that result, the sample was compressed to a smaller thickness and retested at 69kPa of pressure. This was repeated until the sample had been compressed under 655kPa of pressure. This allowed for a constant pressure test of 69kPa to be carried out using the same sample under different thicknesses. The 25 micron fiber samples were tested under 69kPa, 138kPa, 275kPa and 414kPa of constant pressure in separate tests. The results can be seen in Figure 3-12.
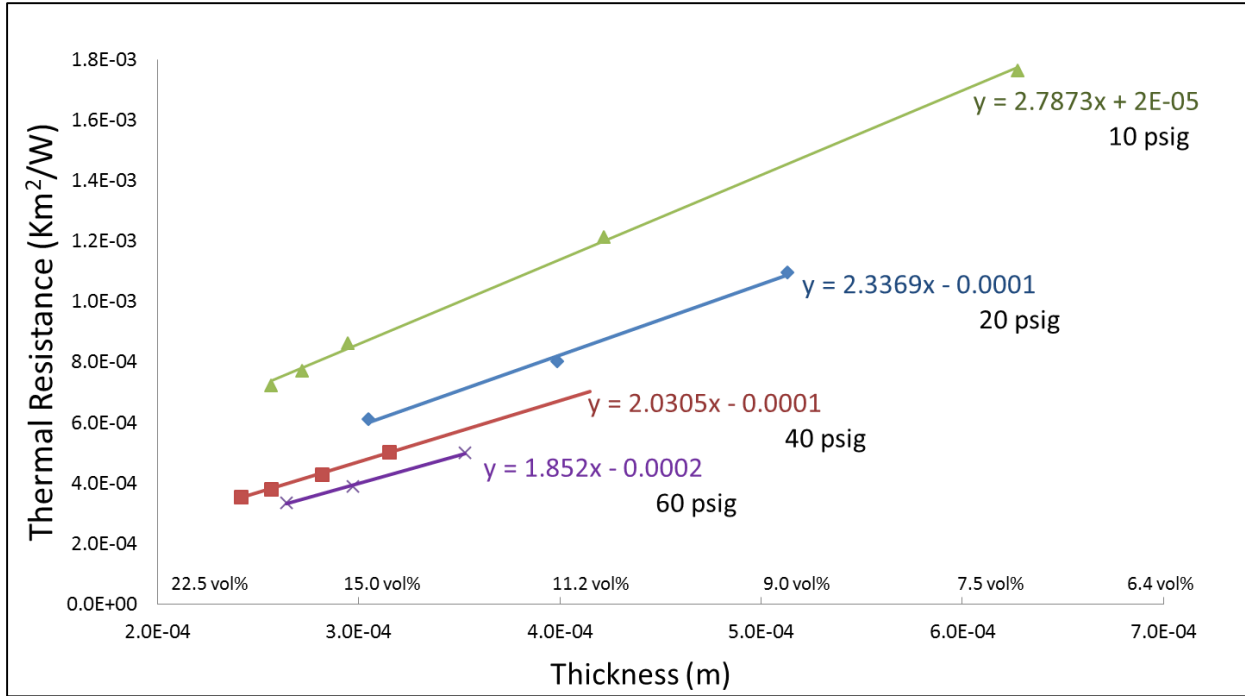
Figure 3-12 - Constant pressure TIM tests for 25 micron fiber MFEC. Tested using TIM Tester with sample held at 50°C. Each individual pressure test was run with the same sample.

The equation of each line in Figure 3-12 follows the following format in Equation (3.12).

$$R_{\text{bulk}} = \frac{1}{k}x + 2R_{\text{contact}} \tag{3.12}$$

Where x is the sample thickness.

Plotting the thermal conductivity versus contact pressure will determine the linearity of how a sample's thermal conductivity changes with pressure. This result is seen in Figure 3-13.
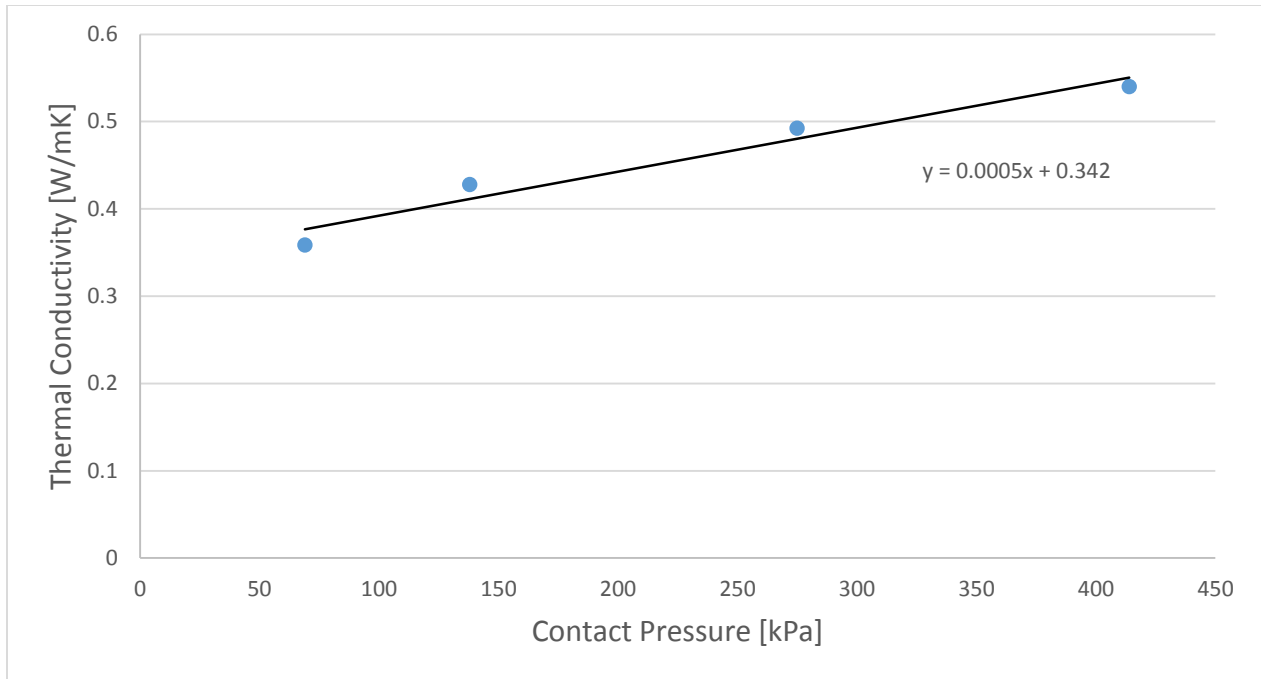
Figure 3-13 - Axial thermal conductivity of MFEC versus contact pressure. This data was extracted from Figure 3-12.

Figure 3-13 shows that the MFEC has a linear thermal conductivity change with contact pressure. In order to minimize this effect, all MFEC samples were compressed with 655 kPa of pressure to create the contacts and maintain a constant thickness of the MFEC for the remainder of the TIM tests.

For the following tests, aluminum (Alloy 1199) disks were manufactured to represent a surface that could have varying degrees of "roughness" or increased surface area by milling out part of the surface. Three disks were made, the first was smooth (3200 grit sand paper polish), the second was milled with a triangular bit (45 deg) to a depth of 0.76 mm and the third was milled with the same triangular bit to a depth of 1.52 mm. The milled out area increased the surface area of the second and third disk by 32% and 64% respectively for the amount of material that was removed. A representation of the roughened disks can be seen in Figure 3-14.
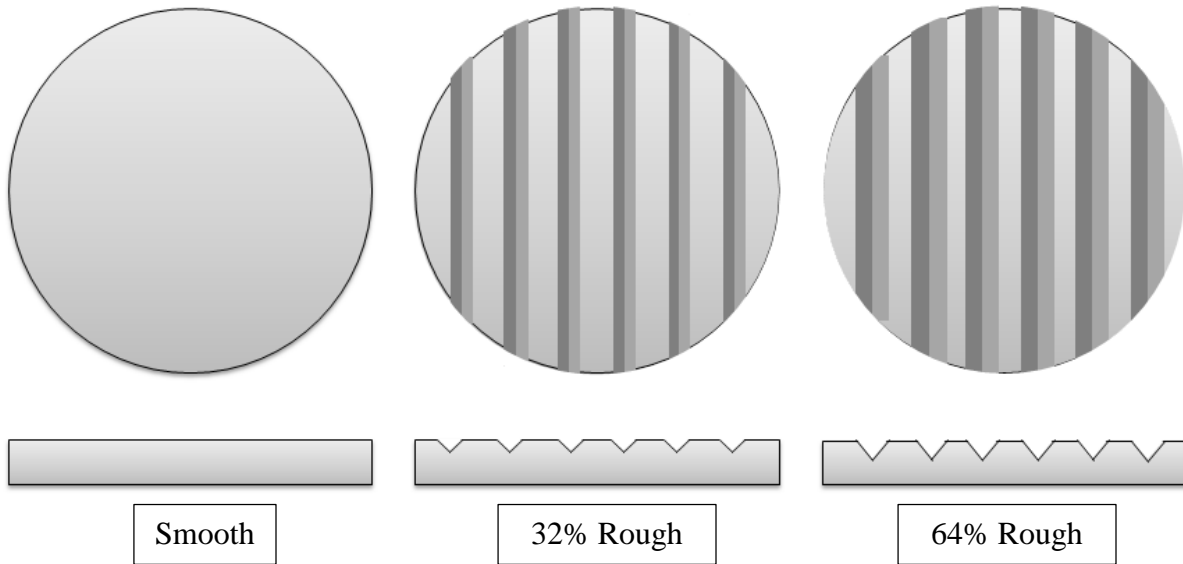
Figure 3-14 - Representation of the roughened disks used in the TIM tests. The percent roughness is shown to identify each specific disk as it was tested.

For these tests, a small amount of oil was placed between the testing surface of the TIM tester and the aluminum disk to lower the thermal resistance. The roughened (or smooth) side was placed side up and the MFEC was placed directly on top of the aluminum disk. The TIM tester stage was lowered onto the MFEC and the sample was compressed at 655 kPa to ensure that the MFEC deformed to the surface of the aluminum disk. The samples were tested at 34, 69, 103 and 138 kPa. A schematic of the setup can be seen in Figure 3-15. The results can be seen in Figure 3-16, Figure 3-17 and Figure 3-18.
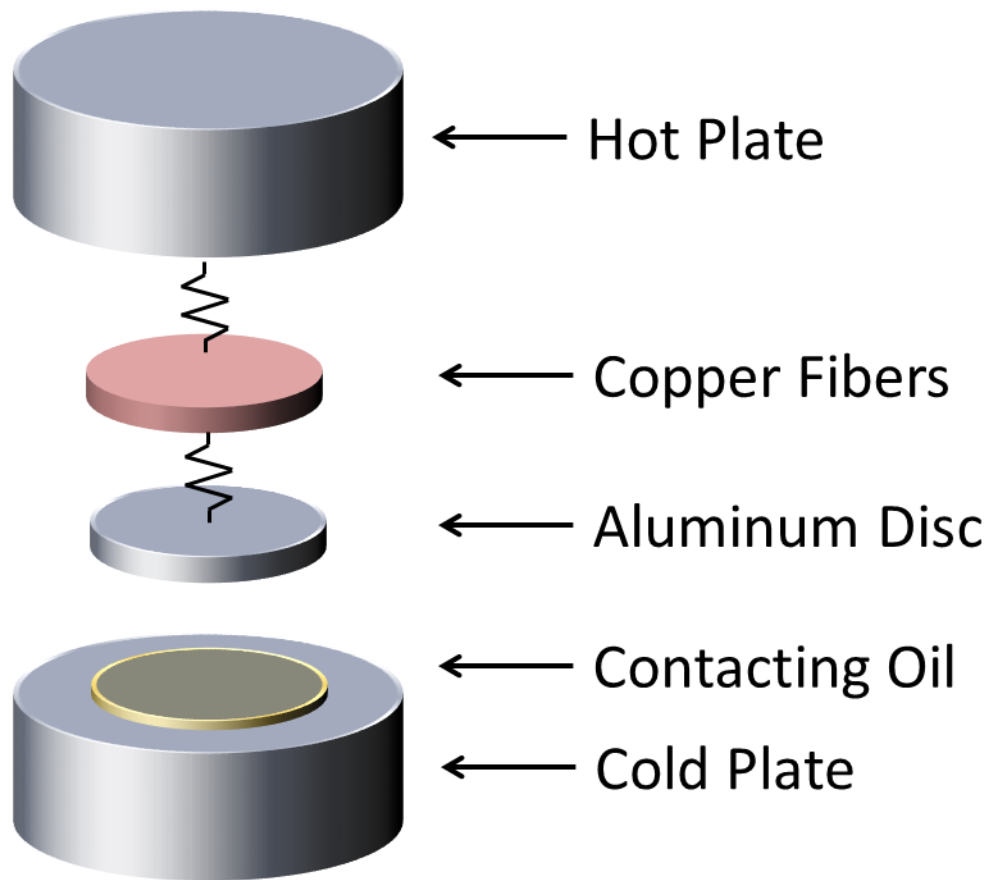
Figure 3-15- Schematic of TIM Tester setup with roughened aluminum discs.
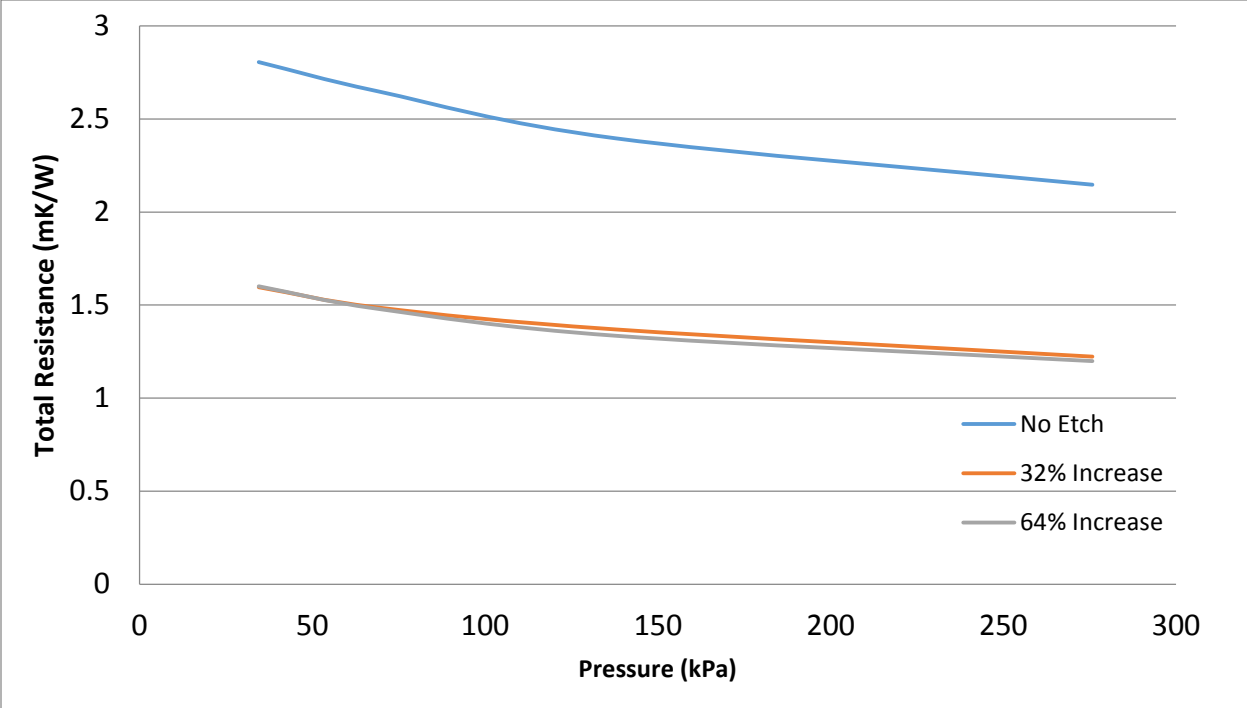
Figure 3-16 - Aluminum disk test with 6 micron fiber MFEC. Tested using the TIM tester. Three samples of similar density and thickness were tested to acquire these results. One sample was tested with each individual aluminum disk. Samples held constant at 50°C. A diagram of each disk can be seen in Figure 3-14.
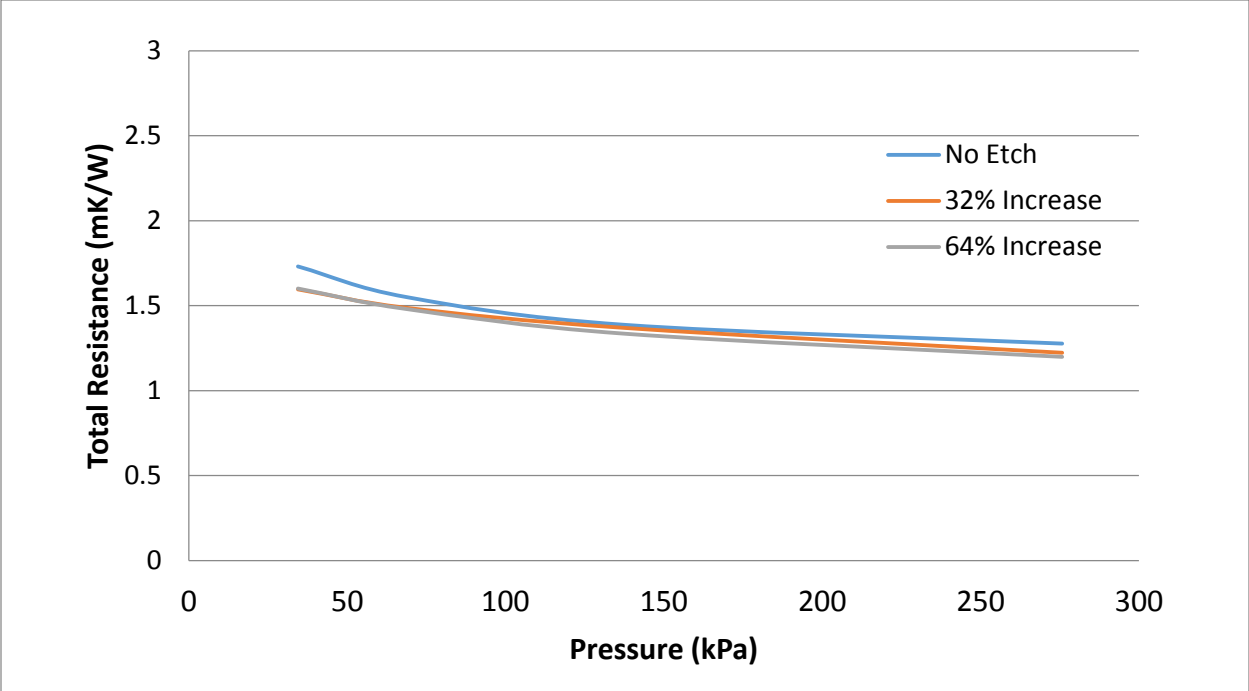
Figure 3-17 - Aluminum disk test with 12 micron fiber MFEC. Tested using the TIM tester. Three samples of similar density and thickness were tested to acquire these results. One sample was tested with each individual aluminum disk. Samples held constant at 50°C. A diagram of each disk can be seen in Figure 3-14.
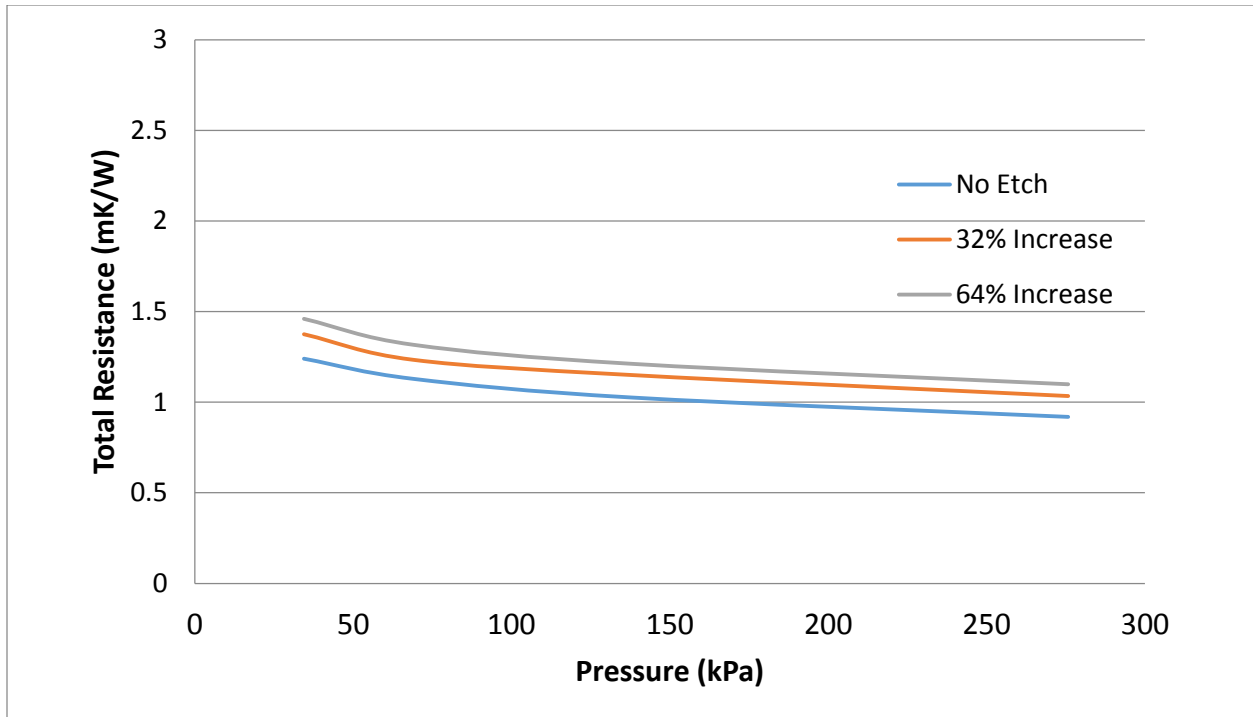
Figure 3-18 - Aluminum disk test with 25 micron fiber MFEC. Tested using the TIM tester. Three samples of similar density and thickness were tested to acquire these results. One sample was tested with each individual aluminum disk. Samples held constant at 50°C. A diagram of each disk can be seen in Figure 3-14.

One additional experiment was run with the MFEC to test the effect of blending various fiber diameters together. Table 3-10 shows the various fiber blends that were created for this experiment. The samples were all tested at a constant pressure of 275 kPa. The average thickness of each sample was approximately 0.47±0.09mm. The results from this test can be seen in Figure 3-19.

Percent Composition [%]			
Fiber Blend	6 Micron	12 Micron	25 Micron
1	100	0	0
2	50	50	0
3	0	100	0
4	0	50	50
5	0	0	100
6	50	0	50
7	33	33	33

Table 3-10 - Fiber blends for TIM testing. The results of these tests can be seen in Figure 3-19.
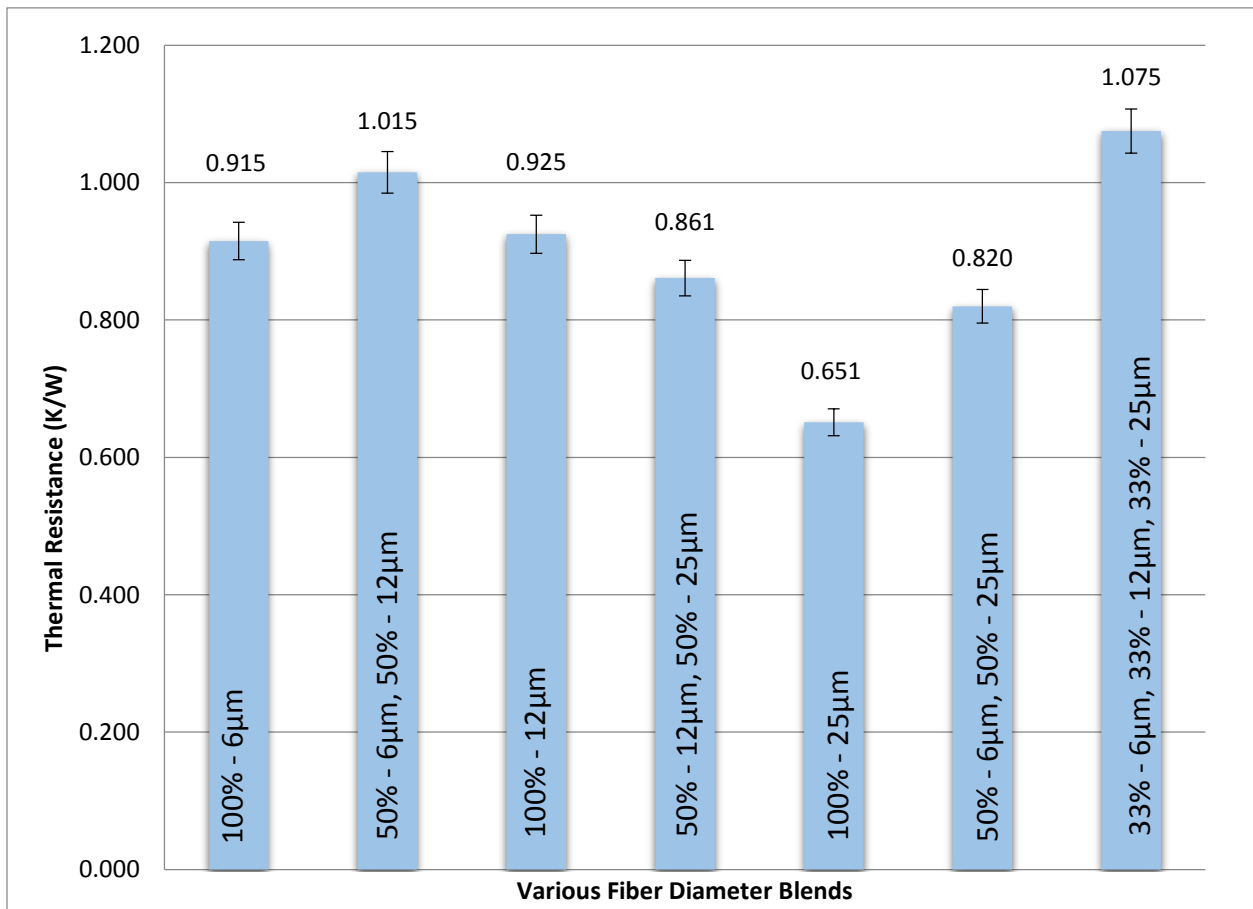
Figure 3-19 - Bulk thermal resistance for various blends of copper fibers.   The copper fiber diameters were blended on a mass basis.

These results will be discussed further in Section 4.3.

3.7 Thermal Conductivity Tester Experiments

The thermal conductivity tester was used as a non-destructive method for obtaining the axial thermal conductivity of the MFEC. Samples were placed directly on top of the sensor. Since the device is capable of making many measurements within a short period of time, 6 samples were taken and averaged together to give the following results seen in Figure 3-20.
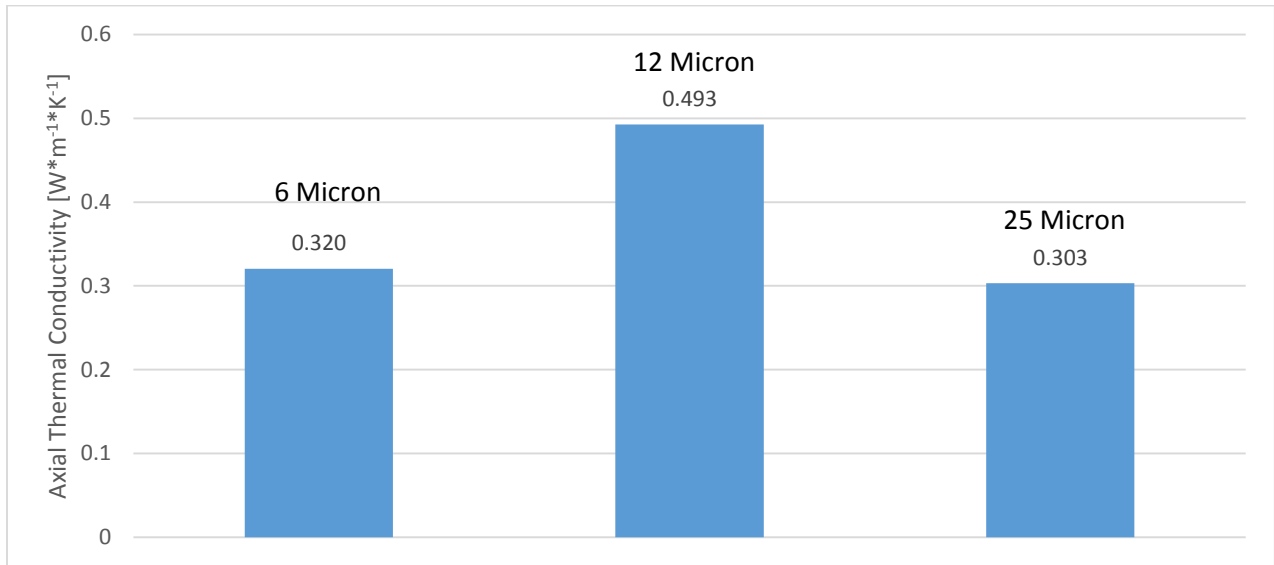
Figure 3-20 - Axial thermal conductivity measurements from thermal conductivity tester. Samples were all compressed under a uniform pressure in preparation for this test. Therefore the vol% of the fibers will be different among all of the fiber diameters.

These results will be discussed further in Section 4.5.

3.8 Resistance Network Diagrams for Experimental Results

Resistance network diagrams are commonly used to describe heat transfer scenarios that involve parallel and series "pathways" for the heat to pass through. For the case of the MFEC in the radial heat transfer tests, the heat could pass from the wall into the MFEC by solid-solid contact with a fiber, through the interstitial fluid gap or by convection. For simplicity, the only two pathways considered in these experiments will be the conduction pathways through the interstitial fluid and solid-solid contact with the wall. The resistance network diagram for the tube experiments would look like the one in Figure 3-21.
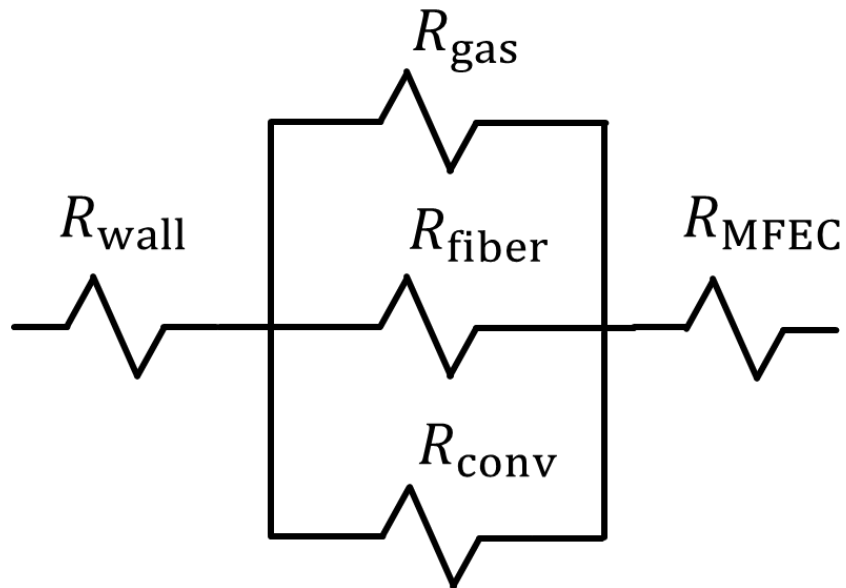
Figure 3-21 - Resistance network diagram for the MFEC-tube wall interface. The interstitial fluid resistance is noted by "R_gas", the solid-solid fiber contact is noted by "R_fiber" and any convective element is noted by "R_conv".

For non-convective boundary pathways, the general formula for each resistance is defined by Equation (3.13). The radial coordinate system would use a resistance term seen in

Equation (3.14). For convective boundaries or resistive boundaries, the resistance term is

defined in Equation (3.15), with the radial component defined in Equation (3.16).

$$R = \frac{\Delta x}{kA} \tag{3.13}$$

$$R = \frac{A_o \ln(r_o/r_i)}{2\pi kL} \tag{3.14}$$

$$R = \frac{1}{hA} \tag{3.15}$$

$$R = \frac{A_o}{A_i}\frac{1}{h} \tag{3.16}$$

Using these equations, the individual resistances can be extracted from the bulk parameters

obtained from experiments. Using data from the 12 micron smooth tube experiments, an

example calculation is demonstrated below:

$$R_{\text{wall}} = \frac{A_o \ln(r_o/r_i)}{2\pi k_{\text{wall}}L}$$

$$R_{\text{gas}} = \frac{A_o \ln(r_o/r_i)}{2\pi k_{\text{gas}}L}$$

$$R_{\text{fiber}} = \frac{A_o \ln(r_o/r_i)}{2\pi k_{\text{fiber}}L}$$

$$R_{\text{MFEC}} = \frac{A_o \ln(r_o/r_i)}{2\pi k_{\text{MFEC}}L}$$

Since the tube wall resistance remains a constant through all tests, its value is determined to be

2.07E-4 K/W. Using the data from the radial heat transfer, the results in Table 3-11, Table 3-12

and Table 3-13 were obtained.

Thermal Resistance [K·W^{-1}]		
Interstitial Fluid	R_{gas}	R_{fiber}
Rough Vacuum (<500 torr)	INF	4.12 E-6
Krypton	1.39 E-3	4.16 E-6
Argon	7.39 E-4	3.77 E-6
Nitrogen	4.70 E-4	3.54 E-6
Neon	2.67 E-4	3.17 E-6
Helium	8.38 E-5	2.64 E-6
Hydrogen	7.19 E-5	2.37 E-6

Table 3-11 - Thermal resistances of interstitial fluid for radial heat transfer tests. These tests used 6 micron fibers (8.8 vol%).

Thermal Resistance [K·W^{-1}]		
Interstitial Fluid	R_{gas}	R_{fiber}
Rough Vacuum (<500 torr)	INF	3.58 E-6
Krypton	1.39 E-3	3.45 E-6
Argon	7.39 E-4	2.86 E-6
Nitrogen	4.70 E-4	2.62 E-6
Neon	2.67 E-4	2.40 E-6
Helium	8.38 E-5	1.98 E-6

Table 3-12 - Thermal resistances of interstitial fluid for radial heat transfer tests. These tests used 12 micron fibers (8.8 vol%).

Thermal Resistance [K·W^{-1}]		
Interstitial Fluid	R_{gas}	R_{fiber}
Rough Vacuum (<500 torr)	INF	3.91 E-6
Krypton	1.39 E-3	4.14 E-6
Argon	7.39 E-4	3.07 E-6
Nitrogen	4.70 E-4	3.20 E-6
Neon	2.67 E-4	2.42 E-6
Helium	8.38 E-5	1.93 E-6
Hydrogen	7.19 E-5	1.92 E-6

Table 3-13 - Thermal resistances of interstitial fluid for radial heat transfer tests. These tests used 25 micron fibers (8.8 vol%).

The "INF" result for R_{gas} indicates that there was no heat flow through the interstitial gas gap due to the absence of any fluid in the vacuum. It can be shown that for the Hydrogen and Helium tests, that the thermal resistance of the wall was the limiting step in heat transfer. These results will be discussed further in Section 4.6.

4. DISCUSSION OF RESULTS

4.1 Radial Temperature Discussion

The test results from the radial temperature analysis display a variety of interesting trends. Looking specifically at the effect of the fiber diameter on both the wall heat transfer coefficients and effective thermal conductivity, it can be shown that there is generally an increase from 6 micron to 12 micron, but a decrease from 12 micron to 25 micron. While there are some exceptions to the trend, the decrease from 12 micron to 25 micron was directly related to the poor sintering of the 25 micron fibers. Figure 4-1, Figure 4-2 and Figure 4-3 show representative sinter-junctions within the sintered fiber network of copper fibers.
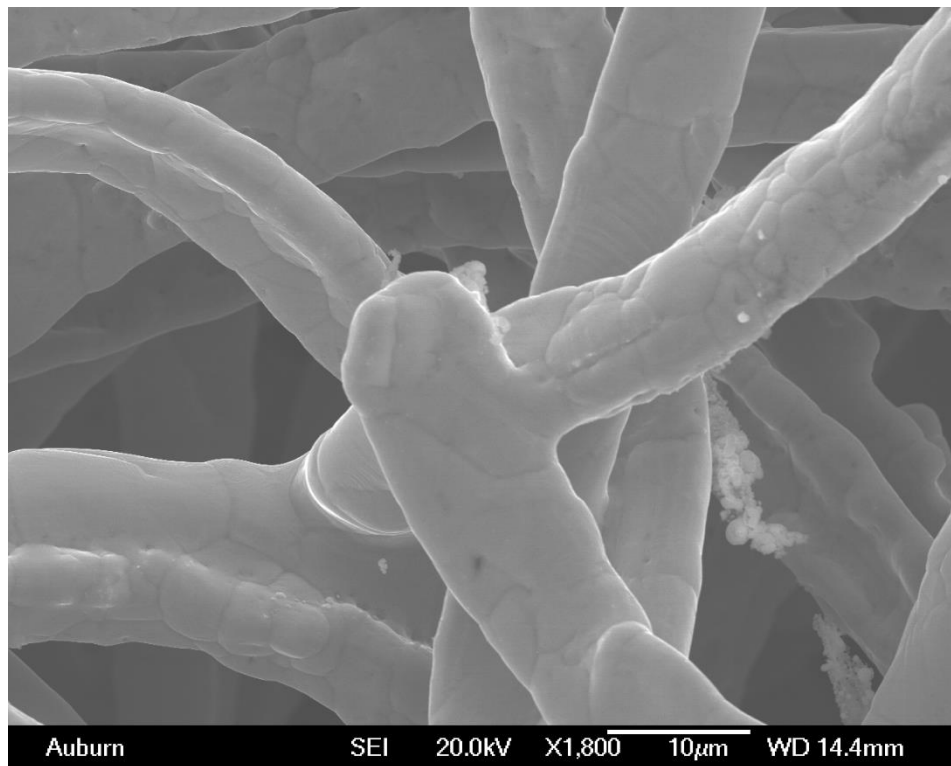
Figure 4-1 - SEM image of representative sinter junctions of 6 micron MFEC. Sintered at 800°C for 36.7 minutes.
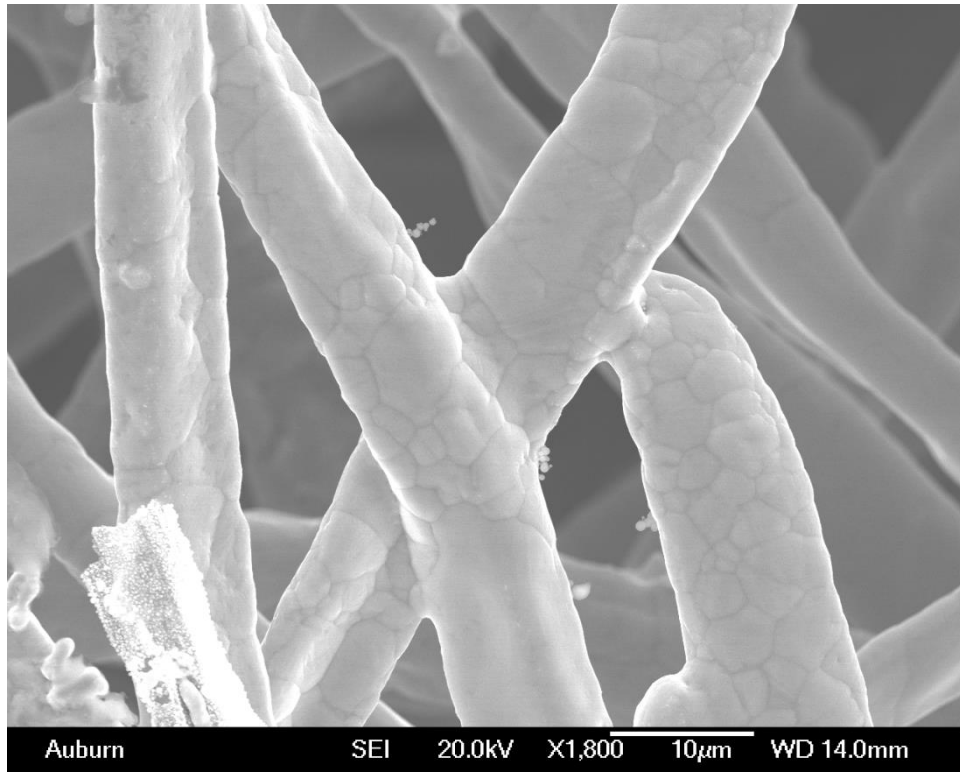
Figure 4-2 - SEM image of representative sinter junctions of 12 micron MFEC. Sintered at 800°C for 36.7 minutes.
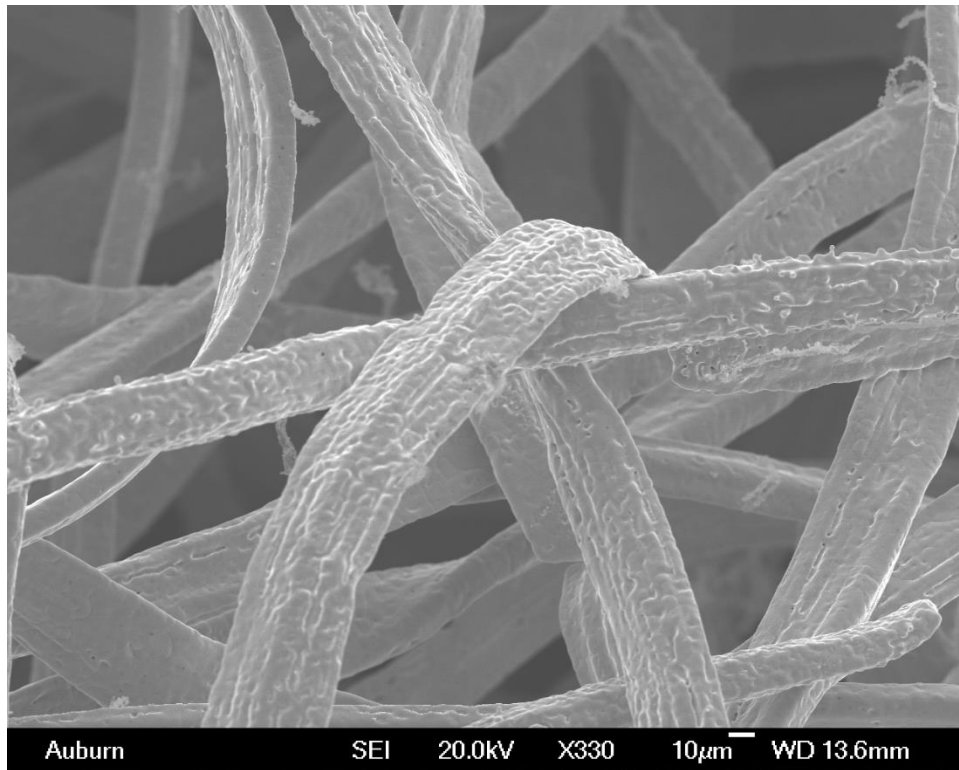
Figure 4-3 - SEM image of representative 25 micron fibers lacking good sinter junctions. Sintered at 800°C for 36.7 minutes.

While examining the 25 micron fibers, no observable sinter junction could be found. Sheng determined that one of the most important factors in heat transfer through small metal fibers was the amount of sintering between the fibers [21]. Since the 25 micron fibers were not well sintered, the hypothesis of greater fiber diameter correlating to higher effective thermal conductivity will not be correctly tested. However, to maintain a consistent basis to compare all fiber types, the sintering temperature and time were held constant across all fiber diameters.

Looking at the general trend of effective thermal conductivity, it can be shown that by increasing the thermal conductivity of the interstitial fluid the effective thermal conductivity increases. One exception to this trend can be seen with the use of Krypton. This result was

surprising but was repeatable and tested to not be a mathematical anomaly. The most probable explanation for this occurring is that Krypton has a high heat capacity (the product of density and heat capacity) and low thermal conductivity compared with many other monatomic gases tested. Therefore Krypton acts more as an insulator that inhibits the transfer of heat by absorbing heat and transferring it poorly. This can cause the small gaps that exist between the fibers to become thermal bottlenecks that would more efficiently transfer heat if they were left empty (as can be seen by the vacuum experiment). It can be hypothesized that gases with lower thermal conductivity than Krypton (SF_6 and Xe) would produce the same type of effect.

The increase in the effective thermal conductivity with increasing thermal conductivity of the interstitial fluid shows how important the interstitial fluid is to the effective thermal conductivity. Since the interstitial fluid makes up over 90% by volume of the MFEC, it is an extremely important part. Even in the poorly sintered 25 micron fibers, the effective thermal conductivity doubles from vacuum to helium. However, this effect was only observed in gases. Should a liquid with a higher thermal conductivity be placed within the fiber matrix, it may not necessarily contribute to a higher effective thermal conductivity. Since liquids are far denser than gases, their contribution to the bulk heat capacity would be much greater.

For the wall heat transfer coefficient analysis, it can be seen that an increase in interstitial fluid thermal conductivity leads to a higher wall heat transfer coefficient. For the case where a rough vacuum was used, the only path for heat to transfer into the MFEC would be by the copper fibers in contact with the wall (assuming that radiation heat transfer is negligible). A good hypothesis to make before analyzing these results would be that there exists an optimal balance between the fiber diameter and the amount of contact with the wall. For example, the smaller the fiber diameter, there will be more fibers in contact with the wall. However, the increase in fibers

contacting the wall doesn't mean that the heat will be able to be transferred fast enough through the smaller fibers. Assuming that the 25 micron fibers in contact with the wall provide a good basis for a well sintered fiber matrix, it can be observed that 12 micron fibers are more efficient at transferring heat than either the 6 or 25 micron. This is most likely due to the 12-micron fibers having a good balance between the amount of contact and ability to transport heat away from the wall.

Another interesting point to make is that the interstitial fluid plays a significant role in the heat transfer at the wall. If a good approximation of wall contact would be the metal volume percent of the MFEC, it would conclude that approximately 90% of the wall heat transfer area is exposed to the interstitial fluid. For a milled copper surface solid-solid contact under vacuum a heat transfer coefficient of 11360 W/m^2K [24]. This value represents 100% solid-solid contact under 7-70 atm of contact pressure with a roughness of 10μm. For the MFEC a value of 1067 W/m^2K is observed for 12 micron fibers under vacuum. Assuming the only heat path is through the fibers then the effective area in contact would be 9.39%. This value is very close to the actual value of 8.8 vol%. Another additional factor is the over-size on the punch allows for the fibers to compress and conform to the surface of the tube wall. Therefore it is reasonable to assume that 9.3% of the wall is in good solid-solid contact with the copper fibers. However, this does not account for any thermal bottle-necks that could occur within the fibers that may affect the wall heat transfer coefficient. For example, 6-micron fibers show a 7.5% contact and the 25-micron fibers show a 6.3% contact. While all three fiber types were packed into the tube identically, this difference may not be a true indication of solid-solid contact, but rather an optimal amount of surface area contact and effective thermal conductivity of the MFEC.

The last point worth discussing is that the results are the solution to a least-squares best-fit analysis. Both the effective thermal conductivity and the wall heat transfer coefficient are linked numerically in the overall solution. While it is possible to perform a sensitivity analysis on each individual component to determine the magnitude of the effect, it is impossible to solve for one variable without simultaneously solving for the other. For this reason, the external heat transfer coefficient was fixed to remove another degree of freedom from the simulation. These assumptions may have altered the accuracy of the results, but it allowed for more precise and repeatable results that could lead to the analysis of the trends present in the experiments.

4.2 Roughened Tube Wall Discussion

The test results for the roughened tube wall experiments show an interesting trend. It was hypothesized that the increase in surface area would give rise to higher wall heat transfer coefficients. However, the results show that roughening the wall of the tube only lowers the wall heat transfer coefficient. The problem with the packing method used in these experiments is that the roughened wall plastically and irreversibly bent the fibers upon entry into the tube. Therefore, the fibers were unable to make good solid-solid contacts due to the deformation of the soft fibers. Had the fibers acted more elastically, perhaps the fibers would have made better contact with the roughened wall. Other materials such as stainless steel would behave more elastically than copper and would be a better candidate for this type of testing. From Section 2.6, it was determined that the sintering process softened the material by annealing the cold worked fibers, and as discussed in Section 1.3, a soft material that deforms against a smooth surface provides much better contact conductance than a soft material that weakly conforms to a roughened surface.

A better approach to roughening the walls would be to cut grooves that traverse the length of the tube without any twist. This way the deformation that occurs would conform the entire length of the tube wall. Perhaps it would be possible to create a tube that was extruded with the grooves in the tube wall. This additional surface area would help enhance the amount of heat that can enter the MFEC at the tube-MFEC interface. The important point to take away from these experiments is that a screw-like pattern requires that the MFEC be "twisted" precisely as it is loaded into the tube. Since the MFEC was not twisted as it was packed into the tube, the experimental results reflect that the MFEC was damaged as it was placed into the tube and prevented the additional surface area from being utilized as well as preventing good solid-solid contact with the wall from occurring.

4.3 Flowing Gas Experiments Discussion

The flowing gas tests were performed to test the MFEC's ability to transfer heat to and from the surrounding fluid as it passes through the fiber network. In the experimental case of gas flowing at 0.22 m/s, the heat transfer coefficients for the MFEC averaged around 260 [W/m^{2}K], which was a 5-6 fold increase over the blank tube test of 44.9 [W/m^{2}K]. The trend in the data that is interesting is that increasing the flow rate in the MFEC increases the outlet temperature. This is not observed within the smooth tube. The reason for this increase is most likely due to all of the copper fibers acting a small "fins" with a large amount of surface area. While it seems that each individual fiber diameter performed similarly, the metal volume percent is most likely the most important factor in the MFEC.

4.4 Thermal Interface Material Tester Discussion

The several tests that were run with the TIM tester reveal a tremendous amount of information about the behavior of the MFEC's axial thermal properties. Since the MFEC cannot

easily be tested radially with the TIM Tester, the axial component was the chosen property for these tests. In the wet-lay preparation of the MFEC, it is important to note that the fibers are preferentially oriented in the radial direction which yields lower axial thermal conductivity values compared to radial thermal conductivity values. The approximate ratio between radial thermal conductivity and axial conductivity can range from 10:1 to 14:1.

The first experiment conducted were the constant pressure tests. The results from this experiment showed that the MFEC (25 micron fibers) creates additional solid-solid contacts with fibers as it is compressed. While these types of materials are discouraged from being used for determining contact resistances, they provide very valuable information about a material's thermal conductivity. The results from the constant pressure tests showed that the thermal conductivity of 25 micron fibers under no contact pressure (extrapolating the linear fit in Figure 3-13) gave a value of 0.342 $Wm^{-1}K^{-1}$. In Section 3.7, the thermal conductivity of the 25 micron fibers (tested with the Thermal Conductivity Tester) gave a value of 0.303 $Wm^{-1}K^{-1}$. Since the TIM test value will give an overestimate due to the behavior of the copper fibers under pressure it is reasonable to confirm that both methods give an accurate measurement of the axial thermal conductivity for the MFEC.

For the milled aluminum disk tests, the objective for this test was to test an alternative approach to the roughened tube wall test performed in Section 3.4. Since the fibers were oriented in a different direction and the deformation against the wall would be non-destructive as discussed in Section 4.2, it provided a useful insight to each fiber diameter's ability to deform against a milled out surface. Since the tests were performed under pressure (no pressure was applied in the roughened tube test), the fibers had much better contact with each other in the axial direction. This was evident by the 25 micron fibers having a lower overall thermal

resistance than the 12 micron fibers and 6 micron fibers. Since the fibers followed this trend, the various disks revealed how the various fiber diameter MFEC samples would conform/deform to the surface of the aluminum disk.

The results show that the 6 micron fibers exhibited a large improvement with the milled surfaces, but were relatively unaffected by the amount of surface area increase. The 12 micron fibers did not exhibit a noticeable increase or decrease with the milled out disks. The 25 micron fibers exhibited a larger resistance with the milled out disks. This confirmed that smaller fibers are able to conform/deform more to a surface than larger diameter fibers. A representation of this can be seen in Figure 4-4. It is hypothesized the reason for this trend could be from two (or both) sources. First, it is easier to bend and deform a smaller diameter wire/fiber. Second, the smaller fibers created more contacts with the milled out surface due to the number of fibers per unit volume. For example, at the same density, there are 17.4 times the number of 6 micron fibers than 25 micron fibers. This allows for a greater chance that the 6 micron fibers made solid-solid contact with the milled area. These experiments show that for a fiber diameter greater than 12 microns, a smooth surface will allow for a lower overall thermal resistance and that for fibers smaller than 12 microns in diameter a roughened surface may be a suitable choice for a decrease in thermal resistance.
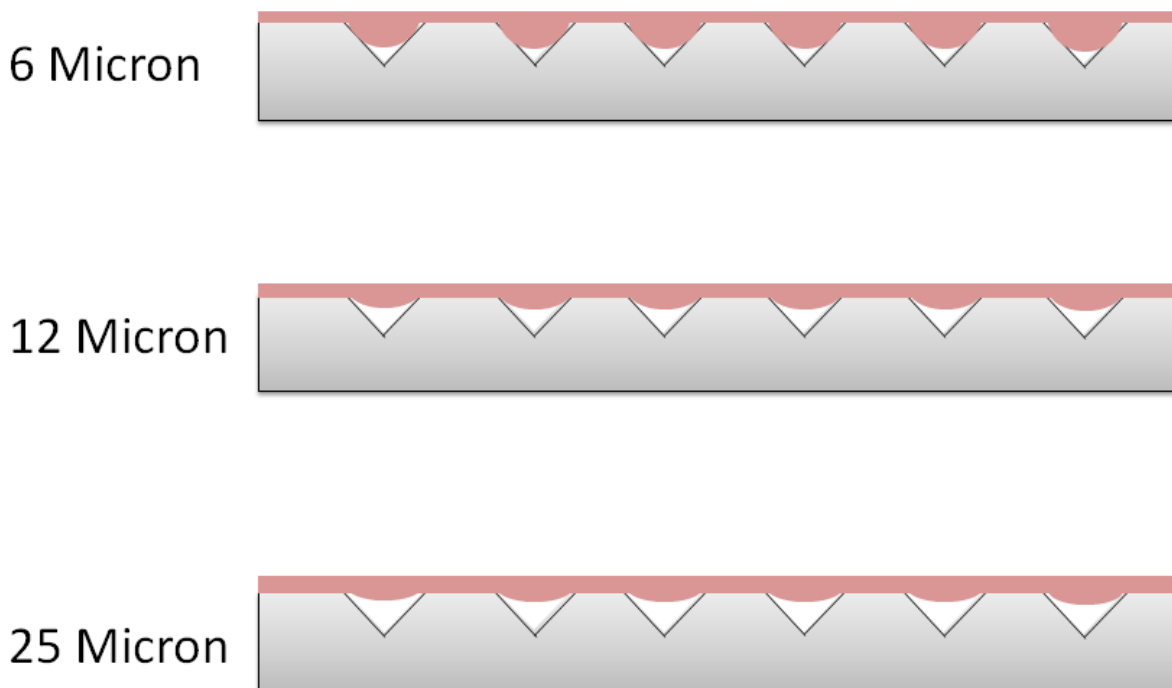
Figure 4-4 - Representation of the fibers conforming to the aluminum disks. Larger diameter fibers will deform less than smaller diameter fibers.

Finally, various fibers were blended together to test the hypothesis that various fiber diameters could make the MFEC structure multi-functional. For example, the 25 micron fibers could be the large heat pipes to transport heat to smaller fibers that would be capable of holding small catalyst particles. The various fiber blends were tested to see if there was an optimal mixture. From Figure 3-19, it can be observed that the larger the mean fiber diameter, the lower the overall thermal resistance. The only exception to this is the tertiary blend of equal parts of each fiber diameter. This test helps to confirm the aluminum disk test showing that increasing fiber diameter leads to a lower thermal resistance (with applied pressure). This test also shows the ability of small diameter fibers (12 and 6 micron) to deform against a roughened surface to lower or maintain the overall thermal resistance.

4.5 Thermal Conductivity Tester Discussion

The thermal conductivity tester proved to be a valuable test to confirm the assumptions made about the poor sintering junctions within the 25 micron fibers seen in Figure 4-3. Since the 25 micron fibers had a lower thermal resistance than the 12 and 6 micron fibers in the TIM tests, it was concluded that the fibers were compressed and allowed to create additional solid-solid contacts that enhanced its axial thermal conductivity. Since the fibers were not under pressure in the tube tests, these thermal conductivity tests help provide the explanation for the lower-than hypothesized thermal conductivity seen in the tube tests using 25 micron fibers.

4.6 Thermal Resistance Network Diagram Discussion and Conclusion

From the thermal resistance network diagrams, the limiting step in the radial heat transfer experiments can be quantified. For the majority of the interstitial fluids (all except for Helium and Hydrogen), the interstitial fluid was the limiting step in the heat transfer. This point is worth discussing due to the applications the MFEC has. Since one of its primary functions is to serve as a catalyst support structure for SynGas (2:1 ratio of H_2 to CO, Thermal Conductivity $= 0.122$ [$Wm^{-1}K^{-1}$]) based reactions, the wall resistance will be the limiting step. This means that the only way to improve radial heat transfer in a stainless steel reactor will be to reduce the resistance of the wall by increasing the amount of surface area or improving the amount of solid-solid contacts with the MFEC.

5. CONCLUSIONS AND RECOMMENDATIONS

5.1 Recommendations for Future Work

Some recommendations for future experiments are listed below:

1) Study the effect of volume percent of fiber on the effective radial thermal conductivity.

2) Conduct TIM tests for various fibers to determine the effect of pressure on the axial thermal conductivity.

3) Test the effect of heat removal by adding a heat generation source within the MFEC.

4) Test tubes that have milled area that do not have a twist or threading to them.

5) Couple the use of foils, greases or screens with the MFEC to enhance the heat transfer properties at the MFEC to tube wall interface.

5.2 Conclusions

In conclusion of these studies, many trends and insightful information were gathered from all of the experiments performed. The main objectives of the study were to extract thermal parameters from the bulk MFEC properties. With the vacuum experiments, the contributions of the individual fibers were isolated and quantified as seen in Table 3-3. By varying the interstitial fluid thermal conductivity, the interstitial fluid's contribution to the effective thermal conductivity was also quantified as seen in Table 3-4. The gases chosen span a wide range of possible gas choices that may be used within the MFEC. The wall heat transfer coefficient or contact conductance was also quantified for vacuum as well as various gases. The importance of the wall to interstitial fluid gap was calculated to be the limiting step for a stainless steel tube wall. Gas thermal conductivities above helium were found to reduce the limiting step to the wall during the radial transient heat transfer tests. Since smaller fibers create more contact points with the wall than larger fibers, the interstitial fluid's contribution to the wall heat transfer coefficient is greater with larger fibers.

For the roughened tube experiments, the results in Section 4.4 clearly indicate that the copper fibers did not have enough elasticity to resist being permanently damaged as they were packed into the tube. The increased elasticity was evaluated and quantified using the hardness testing method outlined in Section 2.6. Had the tube been cut without any twist in the grooves perhaps this additional surface area would have shown improvement. Since the fibers were damaged, the amount of solid-solid contacts was decreased by up 50% or more as shown by the vacuum tests. Dimensionality needed to be considered within these tests and tested properly. However, this experiment proved that the MFEC will not pack well into a tube that does not have smooth walls due to the permanent deformation of the copper fibers.

The TIM test results showed insight into the axial behavior of the MFEC. The tube tests were designed to measure the radial properties without consideration of the axial component. The MFEC showed that it responds differently under pressure than with no pressure applied. It was concluded that additional solid-solid contacts were made in the axial direction between the testing surfaces as well as within the MFEC. This was seen clearly in Figure 3-13 as the axial thermal conductivity changed as a function of contact pressure. Also the trend of increasing fiber diameter having a lower thermal resistance was seen in all of the TIM tests performed. The TIM tests also showed that the MFEC could deform to a surface if the fiber diameter was small enough (less than 12 microns in these tests).

The Thermal Conductivity Analyzer results show that axial conductivity without any applied pressure leads to trends seen in the tube tests. It was these tests that helped confirm the hypothesis that the 25 micron fibers were not well sintered. The SEM images further confirmed these results. The Thermal Conductivity Analyzer also helped to verify the results from the TIM tests.

Finally, it can be concluded that these studies provided a useful overview of practical methods that could be used to test the MFEC and obtain qualitative and quantitative results about the MFECs contact with a surface. The percent of wall-to-fiber contact area in the tube was determined and quantified. The contributions of the fibers and interstitial fluid to the effective thermal conductivity and wall heat transfer coefficient were determined. The axial thermal conductivity was quantified and examined to be variable with pressure.

6. REFERENCES

[1] M. E. Dry and H. B. Erasmus, "Update of the Sasol synfuels process," *Annu. Rev. Energy,* vol. 12, pp. 1-12, 1987.

[2] H. Schulz, "Short history and present trends of Fischer-Tropsch synthesis," vol. 186, pp. 3-12, 1999.

[3] R. L. Espinoza, A. P. Steynberg, B. Jager and A. C. Vosloo, "Low temperature Fischer-Tropsch synthesis from a Sasol perspective," *Applied Catalysis A: General,* pp. 13-26, 1999.

[4] R. Krishna and S. T. Sie, "Design and scale-up of the Fischer-Tropsch bubble column slurry reactor," *Fuel Processing Technology,* pp. 73-105, 2000.

[5] B. J. Tatarchuk, H. Yang, R. R. Kalluri and D. R. Cahela, "Microfibrous media and packing method for optimizing and controlling highly exothermic and highly endothermic reactions/processes". United States of America Patent US 20110135543, 9 June 2011.

[6] M. Sheng, H. Yang, D. R. Cahela, W. R. Yantz, C. F. Gonzalez and B. J. Tatarchuk, "High conductivity catalyst structures for applications in exothermic reactions," *Applied Catalysis A: General,* pp. 143-152, 2012.

[7] H.-S. Song, D. Ramkrishna, S. Trinh and H. Wright, "Operating strategies for Fischer-Tropsch reactors: A model-directed study," *Korean Journal of Chemical Engineering,* pp. 308-317, 2004.

[8] K. Muroyama, T. Shimonmichi, T. Masuda and T. Kato, "Heat and mass transfer characteristics in a gas-slurry-solid fluidized bed," *Chemical Engineering Science,* pp. 7406-7413, 13 August 2007.

[9] B. H. Davis, "Fischer-Tropsch synthesis: Overview of reactor development and future potentialities," *Topics in Catalysis,* vol. 32, no. 3-4, pp. 143-168, 2005.

[10] C. V. Madhusudana, Thermal Contact Conductance, New York: Springer, 1996.

[11] E. Fried and F. A. Costello, "Interface Thermal Contact Resistance Problem in Space Vehicles," *ARSJ,* pp. 237-243, 1962.

[12] G. R. J. Cunnington, "Thermal Conductance of Filled Aluminum and Magnesium Joints in a Vacuum Environment.," in *ASME Paper 64-WA/HT-40*, New York, 1964.

[13] B. Koh and J. E. John, "The Effect of Foils on Thermal Contact Resistance," in *ASME-AIChE Heat Transfer Conf.*, New York, 1965.

[14] D. A. Gyorog, "Investigation of Thermal Isolation Materials for Contacting Surfaces," *Prog Astro Aero,* pp. 310-336, 1971.

[15] S. Cividino and M. M. Yovanovich, "A Model for Predicting the Joint Conductance of a Woven Wire Screen Contacting Two Solids," *Prog Astro Aero,* pp. 39:111-128, 1975.

[16] H. J. J. Sauer, C. R. Remington and G. Heizer, "Thermal Contact Conductance of Lubricant Films," *Proc Int Conf Therm Cond,* vol. 11, pp. 24-25, 1971.

[17] K. C. Chung, J. W. Sheffield and T. J. O'Keefe, "Thermal Constriction Resistance of Phase-Mixed Metallic Coatings," *Trans ASME, J Heat Transfer,* vol. 114, pp. 811-818, 1992.

[18] D. K. Harris, D. R. Cahela and B. J. Tatarchuk, "Wet layup and sintering of metal-containing microfibrous composites for chemical processing opportunities," *Composites Part A: Applied Science and Manufacturing,* vol. 32, no. 8, pp. 1117-1126, 2001.

[19] M. Sheng, C. F. Gonzalez, W. R. J. Yantz, D. R. Cahela, H. Yang, D. R. Harris and B. J. Tatarchuk, "Micro scale heat transfer comparison between packed beds and microfibrous entrapped catalysts," *Engineering Applications of Computational Fluid Mechanics,* vol. 4, pp. 471-485, 2013.

[20] S. T. Sie and R. Krishna, "Fundamentals and selection of advanced Fischer-Tropsch reactors," *Applied Catalysis A: General,* vol. 186, pp. 55-70, 1999.

[21] M. Sheng, D. R. Cahela, H. Yang, C. F. Gonzalez, W. R. J. Yantz, D. K. Harris and B. J. Tatarchuk, "Effective thermal conductivity and junction factor for sintered microfibrous materials," *International Journal of Heat and Mass Transfer,* vol. 56, no. 1-2, pp. 10-19, 2013.

[22] M. Sheng, H. Yang, D. R. Cahela and B. J. Tatarchuk, "Novel catalyst structures with enhanced heat transfer characteristics," *Journal of Catalysis,* pp. 254-262, 2011.

[23] W. E. Schiesser and G. W. Griffiths, A Compendum of Partial Differential Equation Models: Method of Lines Analysis with Matlab, Cambridge University Press, 2009.

[24] J. P. Holman, Heat Transfer, New York: McGraw-Hill, 2002.

7. APPENDIX I – MATLAB Code for Radial Thermal Parameter Analysis

Below is the code for the MATLAB simulation that was used in Section 3.2.

```matlab
% Reset
clear all;
clc;

%load data file
load Data_May_21_He_1.mat
Data = Data_May_21_He_1;

% BOUNDS FOR AUTOSOLVE
range_k_high = 100;
range_k_low = 0;
range_h_high = 100000;
range_h_low = 0;

% Parameters to Solve (These need to be "good guesses")
k_eff = 5.6;
k_ss = 16.5;
R = 1750;
h2 = 10000000; %Make this extremely large

% Set Boundary Conditions and Material Properties
T_o = Data(1,4);
T_inf = max(Data(:,5));
rho = 790.871173843012; %VOLUME BASIS
cP = 59;
rho_ss = 7990;
cP_ss = 500;

% Constants
L = 0.01905;
n = 25;
delta_r = L/(n-2);

% Time Settings
delta_t = 1;
time_max = size(Data,1);

alpha = k_eff/(rho*cP);
Fo = alpha*delta_t/(delta_r^2);

alpha_ss = k_ss/(rho_ss*cP_ss);
Fo_ss = alpha_ss*delta_t/(delta_r^2);

error_sum = 0;
range_k = k_eff;
range_h = R;
h_direction = 1;
k_direction = 1;
```

```matlab
%%%% USE Centerline? Pick 4, Else 3
first_thermocouple = 3; %Normally 2
centerline = 4; %Normally 4

for total_loop = 1:700

    solution_found = 0;
    iteration_loop = 0;

    previous_k = k_eff;
    previous_h = R;

    %%%%% Solve for h
    while solution_found == 0

        iteration_loop = iteration_loop + 1;

        % Dimensionalize T and Theta
        T_old = zeros(n,1);

        % Set Slab To Uniform Temperature
        for i = 1:n
            T_old(i,1) = T_o;
        end

        alpha = k_eff/(rho*cP);
        Fo = alpha*delta_t/(delta_r^2);

        % Initialize Matricies
        T_est = T_old;
        A = zeros(n,n);
        d = zeros(n,1);

        % Run Calculations
        iteration_num = 1;

        for time = 1:time_max

            for iteration = 1:50

                % Calculate a, b, c and d for i = 2:(n-1)
                for i = 2:(n-1)
                    for j = 1:(n)

                        r_i = delta_r*(i-1);
                        r_i_w = delta_r*(i-1) - delta_r/2;
                        r_i_e = delta_r*(i-1) + delta_r/2;

                        if i == j
                            A(i,j) = (r_i_w/r_i)*Fo + (r_i_e/r_i)*Fo + 1;
                        elseif i == j-1
                            A(i,j) = -(r_i_w/r_i)*Fo;
                        elseif i == j+1
                            A(i,j) = -(r_i_e/r_i)*Fo;
```

```matlab
            end
            d(i,1) = T_old(i,1);
        end
    end

    % Calculate b, c and d for symmetry boundary
    A(1,1) = 4*Fo + 1;
    A(1,2) = -4*Fo;
    d(1,1) = T_old(1,1);

    % Calculate for SS Wall Middle Node
    r_i = delta_r*(n-2);
    r_i_w = delta_r*(n-2) - delta_r/2;
    r_i_e = delta_r*(n-2) + delta_r/2;

    A(n-1,n) = -(r_i_w/r_i)*Fo_ss;
    A(n-1,n-1) = (r_i_w/r_i)*Fo_ss + (r_i_e/r_i)*Fo_ss + 1;
    A(n-1,n-2) = -(r_i_e/r_i)*Fo_ss;
    d(n-1,1) = T_old(n-1,1);

    % Calculate a and b for convective boundary
    r_i = delta_r*(n);
    r_i_w = delta_r*(n) - delta_r/2;

    A(n,n) = 2*Fo_ss*(r_i_w/r_i) +
(h2/(rho_ss*cP_ss))*(2*delta_t/delta_r) + 1;
    A(n,n-1) = -2*Fo_ss*(r_i_w/r_i);
    d(n,1) = T_old(n,1) +
(h2/(rho_ss*cP_ss))*(2*delta_t/delta_r)*Data(time,5);

    % Calculate a and b for contact of MFM

    r_i = delta_r*(n-3);
    r_i_w = delta_r*(n-3) - delta_r/2;
    r_i_e = delta_r*(n-3) + delta_r/2;

    A(n-3,n-2) = -R/(rho*cP)*(2*delta_t/delta_r);
    A(n-3,n-3) = 2*(r_i_w/r_i)*Fo +
R/(rho*cP)*(2*delta_t/delta_r) + 1;
    A(n-3,n-4) = -2*(r_i_w/r_i)*Fo;
    d(n-3,1) = T_old(n-3,1);

    A(n-2,n-1) = -2*(r_i_e/r_i)*Fo_ss;
    A(n-2,n-2) = 2*(r_i_e/r_i)*Fo_ss +
R/(rho_ss*cP_ss)*(2*delta_t/delta_r) + 1;
    A(n-2,n-3) = -R/(rho_ss*cP_ss)*(2*delta_t/delta_r);
    d(n-2,1) = T_old(n-2,1);


    % Save Old Guess
    T_est_old = T_est;

    % Solve for new T Estimate
    T_est = A\d;        % Using Implicit Method
```

```matlab
            % Check for Convergence
            if abs(T_est - T_est_old) < 1E-5
                %disp(['Iteration number: ', num2str(iteration_num)]);
                %disp(' ');
                %disp(['Time =', num2str(time), 's.']);
                %disp(' ');
                %disp(T_est);
                break
            end
            iteration_num = iteration_num + 1;
        end

%       % Report Values
%       if mod(time,10) == 0
%           disp(['Iteration number: ', num2str(iteration_num)]);
%           disp(' ');
%           disp(['Time =', num2str(time), 's.']);
%           disp(' ');
%           disp(T_est);
%       end

        % Grab Node Values
        T_Predicted(time,1) = time;
        T_Predicted(time,2) = (delta_r*16 -0.01100)*(T_est(16,1) -
T_est(15,1))/(delta_r) + T_est(15,1);
        T_Predicted(time,3) = (delta_r*8 - 0.00635)*(T_est(8,1) -
T_est(7,1))/(delta_r) + T_est(7,1);
        T_Predicted(time,4) = T_est(1,1);

        % Store New Temperature to Old Temperature
        T_old = T_est;

    end

    % Error Analysis for Simulation
    last_error = error_sum;
    error_sum = 0;
    for i = 1:time_max
        for j = first_thermocouple:centerline
            error_sum = error_sum + (T_Predicted(i,j) - Data(i,j))^2;
        end
    end

    % Store Error Data
    error_data(iteration_loop, 1) = error_sum;
    error_data(iteration_loop, 2) = k_eff;
    error_data(iteration_loop, 3) = R;

    % Loop Break
    if iteration_loop > 30
        break
    end
```

```matlab
    % Solve for h
    error_check = (last_error - error_sum);
    h_previous = R;

    if error_check > 0 && (h_direction > 0)
        R = R - 0.1*range_h;
        range_h = range_h*0.7;
    elseif error_check < 0 && (h_direction > 0)
        R = R + 0.1*range_h;
        range_h = range_h*0.7;
    elseif error_check > 0 && (h_direction < 0)
        R = R + 0.1*range_h;
        range_h = range_h*0.7;
    elseif error_check < 0 && (h_direction < 0)
        R = R - 0.1*range_h;
        range_h = range_h*0.7;
    end

    h_direction = (h_previous - R);

end   %%%%% Solve for h

error_sum = 100000;

iteration_loop = 0;

%%%%% Solve for k
while solution_found == 0

    iteration_loop = iteration_loop + 1;


    % Dimensionalize T and Theta
    T_old = zeros(n,1);

    % Set Slab To Uniform Temperature
    for i = 1:n
        T_old(i,1) = T_o;
    end

    alpha = k_eff/(rho*cP);
    Fo = alpha*delta_t/(delta_r^2);


    % Initialize Matricies
    T_est = T_old;
    A = zeros(n,n);
    d = zeros(n,1);
    %T_Predicted = zeros (time_max,n);

    % Run Calculations
    iteration_num = 1;

    for time = 1:time_max
```

```matlab
        for iteration = 1:50

            % Calculate a, b, c and d for i = 2:(n-1)
            for i = 2:(n-1)
                for j = 1:(n)

                        r_i = delta_r*(i-1);
                        r_i_w = delta_r*(i-1) - delta_r/2;
                        r_i_e = delta_r*(i-1) + delta_r/2;

                        if i == j
                            A(i,j) = (r_i_w/r_i)*Fo + (r_i_e/r_i)*Fo + 1;
                        elseif i == j-1
                            A(i,j) = -(r_i_w/r_i)*Fo;
                        elseif i == j+1
                            A(i,j) = -(r_i_e/r_i)*Fo;
                        end
                        d(i,1) = T_old(i,1);
                end
            end

            % Calculate b, c and d for symmetry boundary
            A(1,1) = 4*Fo + 1;
            A(1,2) = -4*Fo;
            d(1,1) = T_old(1,1);

            % Calculate for SS Wall Middle Node
            r_i = delta_r*(n-2);
            r_i_w = delta_r*(n-2) - delta_r/2;
            r_i_e = delta_r*(n-2) + delta_r/2;

            A(n-1,n) = -(r_i_w/r_i)*Fo_ss;
            A(n-1,n-1) = (r_i_w/r_i)*Fo_ss + (r_i_e/r_i)*Fo_ss + 1;
            A(n-1,n-2) = -(r_i_e/r_i)*Fo_ss;
            d(n-1,1) = T_old(n-1,1);

            % Calculate a and b for convective boundary
            r_i = delta_r*(n);
            r_i_w = delta_r*(n) - delta_r/2;

            A(n,n) = 2*Fo_ss*(r_i_w/r_i) +
(h2/(rho_ss*cP_ss))*(2*delta_t/delta_r) + 1;
            A(n,n-1) = -2*Fo_ss*(r_i_w/r_i);
            d(n,1) = T_old(n,1) +
(h2/(rho_ss*cP_ss))*(2*delta_t/delta_r)*Data(time,5);

            % Calculate a and b for contact of MFM

            r_i = delta_r*(n-3);
            r_i_w = delta_r*(n-3) - delta_r/2;
            r_i_e = delta_r*(n-3) + delta_r/2;

            A(n-3,n-2) = -R/(rho*cP)*(2*delta_t/delta_r);
```

```matlab
                A(n-3,n-3) = 2*(r_i_w/r_i)*Fo +
R/(rho*cP)*(2*delta_t/delta_r) + 1;
                A(n-3,n-4) = -2*(r_i_w/r_i)*Fo;
                d(n-3,1) = T_old(n-3,1);

                A(n-2,n-1) = -2*(r_i_e/r_i)*Fo_ss;
                A(n-2,n-2) = 2*(r_i_e/r_i)*Fo_ss +
R/(rho_ss*cP_ss)*(2*delta_t/delta_r) + 1;
                A(n-2,n-3) = -R/(rho_ss*cP_ss)*(2*delta_t/delta_r);
                d(n-2,1) = T_old(n-2,1);


                % Save Old Guess
                T_est_old = T_est;

                % Solve for new T Estimate
                T_est = A\d;          % Using Implicit Method


                % Check for Convergence
                if abs(T_est - T_est_old) < 1E-5
                    %disp(['Iteration number: ', num2str(iteration_num)]);
                    %disp(' ');
                    %disp(['Time =', num2str(time), 's.']);
                    %disp(' ');
                    %disp(T_est);
                    break
                end
                iteration_num = iteration_num + 1;
            end

%       % Report Values
%       if mod(time,10) == 0
%           disp(['Iteration number: ', num2str(iteration_num)]);
%           disp(' ');
%           disp(['Time =', num2str(time), 's.']);
%           disp(' ');
%           disp(T_est);
%       end

            % Grab Node Values
            T_Predicted(time,1) = time;
            T_Predicted(time,2) = (delta_r*16 -0.01100)*(T_est(16,1) -
T_est(15,1))/(delta_r) + T_est(15,1);
            T_Predicted(time,3) = (delta_r*8 - 0.00635)*(T_est(8,1) -
T_est(7,1))/(delta_r) + T_est(7,1);
            T_Predicted(time,4) = T_est(1,1);

            % Store New Temperature to Old Temperature
            T_old = T_est;

        end

        % Error Analysis for Simulation
```

```matlab
        last_error = error_sum;

        error_sum = 0;

        for i = 1:time_max
            for j = first_thermocouple:centerline
                error_sum = error_sum + (T_Predicted(i,j) - Data(i,j))^2;
            end
        end

        % Terminate Search

        % Store Error Data
        error_data(iteration_loop, 1) = error_sum;
        error_data(iteration_loop, 2) = k_eff;
        error_data(iteration_loop, 3) = R;

        if iteration_loop > 45
            break
        end

        % Solve for k_eff

        error_check = (last_error - error_sum);
        k_previous = k_eff;

        if error_check > 0 && (k_direction > 0)
            k_eff = k_eff - 0.1*range_k;
            range_k = range_k*0.8;
        elseif error_check < 0 && (k_direction > 0)
            k_eff = k_eff + 0.1*range_k;
            range_k = range_k*0.8;
        elseif error_check > 0 && (k_direction < 0)
            k_eff = k_eff + 0.1*range_k;
            range_k = range_k*0.8;
        elseif error_check < 0 && (k_direction < 0)
            k_eff = k_eff - 0.1*range_k;
            range_k = range_k*0.8;
        end

        k_direction = (k_previous - k_eff);

end   %%%% Solve for k

clc
disp(['Iteration Number ', num2str(total_loop)]);

range_k = k_eff;
range_h = R;

best_guess = abs(previous_k - k_eff)/k_eff + abs(previous_h - R)/R;

disp(['Total Change ', num2str(best_guess*100), '%']);
```

86

```matlab
    disp(['k = ', num2str(k_eff)]);
    disp(['R = ', num2str(R)]);
    disp(['h2 = ', num2str(h2)]);
    disp(['error = ', num2str(error_sum)]);
    disp(['T_o = ', num2str(T_o)]);
    disp(['T_inf = ', num2str(T_inf)]);

    if best_guess < 0.00005
        disp('SOLUTION FOUND!!!');
        break
    end

    if k_eff > 400000
        disp('Solution Diverged!!!');
        break
    end

    error_sum = 100000;

end
```